

Water-Stable Carborane-Based $\text{Eu}^{3+}/\text{Tb}^{3+}$ Metal–Organic Frameworks for Tunable Time-Dependent Emission Color and Their Application in Anticounterfeiting Bar-Coding

Zhen Li, Rosario Núñez, Mark E. Light, Eliseo Ruiz, Francesc Teixidor, Clara Viñas, Daniel Ruiz-Molina, Claudio Roscini,* and José Giner Planas*



Cite This: <https://doi.org/10.1021/acs.chemmater.2c00323>



Read Online

ACCESS |



Metrics & More

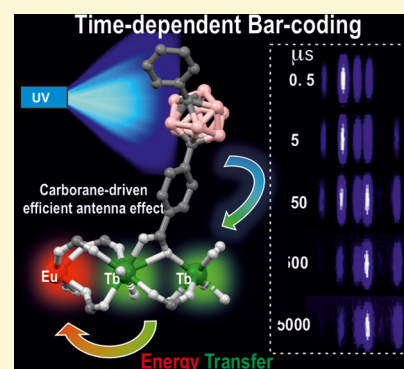


Article Recommendations



Supporting Information

ABSTRACT: Luminescent lanthanide metal–organic frameworks (Ln-MOFs) have been shown to exhibit relevant optical properties of interest for practical applications, though their implementation still remains a challenge. To be suitable for practical applications, Ln-MOFs must be not only water stable but also printable, easy to prepare, and produced in high yields. Herein, we design and synthesize a series of $m\text{CB-Eu}_x\text{Tb}_{1-y}$ ($y = 0-1$) MOFs using a highly hydrophobic ligand $m\text{CBL1}$: 1,7-di(4-carboxyphenyl)-1,7-dicarba-*closo*-dodecaborane. The new materials are stable in water and at high temperature. Tunable emission from green to red, energy transfer (ET) from Tb^{3+} to Eu^{3+} , and time-dependent emission of the series of mixed-metal $m\text{CB-Eu}_x\text{Tb}_{1-y}$ MOFs are reported. An outstanding increase in the quantum yield (QY) of 239% of $m\text{CB-Eu}$ (20.5%) in the mixed $m\text{CB-Eu}_{0.1}\text{Tb}_{0.9}$ (69.2%) is achieved, along with an increased and tunable lifetime luminescence (from about 0.5 to 10 000 μs), all of these promoted by a highly effective ET process. The observed time-dependent emission (and color), in addition to the high QY, provides a simple method for designing high-security anticounterfeiting materials. We report a convenient method to prepare mixed-metal Eu/Tb coordination polymers (CPs) that are printable from water inks for potential applications, among which anticounterfeiting and bar-coding have been selected as a proof-of-concept.



INTRODUCTION

Porous coordination polymers (CPs), also known as metal–organic frameworks (MOFs), are a class of highly crystalline materials formed by metal ions or metal clusters connected by multitopic organic linkers, which have attracted extensive attention over the past few decades.^{1–4} Their large surface areas, framework flexibility, and tunable pore surface properties, as well as “tailor-made” framework functionalities, empower them to be promising candidates for a diverse range of applications.^{2,5–13} Especially interesting is the combination of MOFs with lanthanide (Ln) ions resulting in inherent optical properties, including high luminescence quantum yields, narrow and strong emission bands, large Stokes shifts, long luminescence lifetimes, and an emission wavelength undisturbed by the surrounding chemical environment.^{14,15} Their luminescence is associated with an energy transfer (ET) from the ligand, acting as an antenna, owing to its larger extinction coefficient, to the accepting electronic levels of the emitting lanthanides and it is potentially interesting in a variety of applications, such as e.g., sensors, optoelectronic and in solid-state lighting (SSL) devices, or bioimaging among others.^{16–22} Of particular interest would be the exploitation of emissive Ln-MOFs as optical markers for high-security anticounterfeiting technologies aimed to prevent illegal copies of sensitive identity documents, banknotes,

diplomas, and certificates,^{23–27} which require an ever-increasing tunability (e.g., emission colors) and authentication complexity. However, regardless of the great potential of these materials, to date they have proved unsuitable for practical applications due to their limited chemical^{28–35} and/or optical^{27,36} stability under environmental conditions (e.g., humidity, temperature, etc.).

Herein, we hypothesized that such limitations can be overcome with the introduction of carborane clusters such as icosahedral carboranes $1,n\text{-C}_2\text{B}_{10}\text{H}_{12}$ ($n = 2, 7$ or 12), a class of commercially available and exceptionally stable three-dimensional (3D) aromatic boron-rich clusters that possess material-favorable properties such as thermal/chemical stability and high hydrophobicity.^{37–43} Carborane-based MOFs were first synthesized at Northwestern University, and they showed an increase in their thermal stabilities among other interesting properties.^{44–51} The spherical nature of the carboranes, with

Received: January 31, 2022

Revised: April 19, 2022

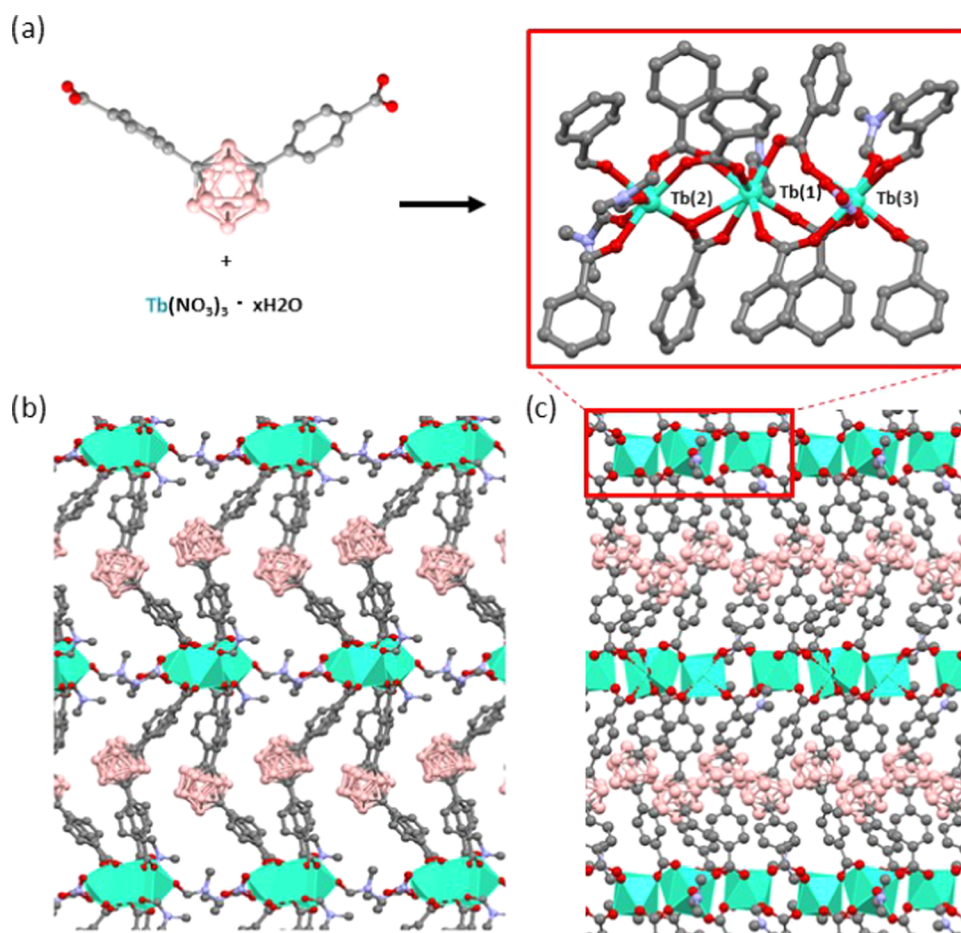


Figure 1. Crystal structure of *mCB-Tb*. (a) View of the coordination of *mCBL1* to the three independent Tb atoms that are repeated along the structure to provide one-dimensional (1D) inorganic rod-shaped chains and (b, c) two perpendicular views of the extended 3D framework along the *b* and *a* axes, respectively. Green polyhedra represent the Tb coordination spheres and H atoms are omitted for clarity. Color code: B, pink; C, gray; O, red; N, dark blue; and Tb, green.

64 slightly polarized hydrogen atoms and the presence of the
65 hydride-like hydrogens at the B–H vertexes, make the
66 carboranes very hydrophobic. Thus, we have recently explored
67 and demonstrated the possibility of increasing the hydrolytic
68 stability of CPs or MOFs by incorporating hydrophobic
69 carborane-based linkers^{52–57} into these porous materials.^{58–63}
70 Our strategy has provided the most water-stable Cu-paddle
71 wheel MOF in the literature, which is related to the high
72 hydrophobicity of the *m*-carborane ligand *mCBL1*: 1,7-di(4-
73 carboxyphenyl)-1,7-dicarba-*closo*-dodecaborane (Figure 1).⁶¹
74 Beyond stability, the delocalized electron density is not
75 uniform through the cage, giving rise to extraordinary
76 differences in the electronic effects of the cluster.⁶⁴ This
77 unusual electronic structure is often highlighted by considering
78 carboranes as inorganic three-dimensional “aromatic” ana-
79 logues of arenes.⁶⁵ In this regard, for the last 25 years, a
80 remarkable influence of icosahedral carboranes on the
81 photophysical properties of organic fluorophores^{66–78} or in
82 their transition metal compounds has been reported.^{57,79–81}
83 However, as far as we know, there are no reports on
84 luminescence properties of carborane-based MOFs⁸² and
85 therefore the antenna effect has not yet been reported for a
86 carborane linker.
87 As a proof-of-concept, in this work, we report the
88 preparation and full characterization of a series of isostructural
89 water-stable *m*-carborane Ln-MOFs,

$\{[(Ln)_3(mCBL1)_4(NO_3)(DMF)_n] \cdot Solv\}$ (*mCB-Ln*, where 90
Ln = **Eu**, **Tb**, or **Eu_xTb_{1-x}**; Figure 1). In addition to their 91
high thermal and water stabilities, the preparation of mixed 92
mCB-Eu_xTb_{1-x}-doped MOFs allowed for fine control and high 93
tunability of both steady-state and time-dependent emission 94
color (from green to red) and lifetime luminescence (from 95
about 0.5 to 10 000 μs). An outstanding increase of 237% of 96
luminescence quantum yield from the single-ion *mCB-Eu* 97
MOF (20.5%) to the mixed *mCB-Eu_{0.1}Tb_{0.9}* MOF (69.2%) is 98
achieved, owing to a highly effective ET process from Tb³⁺ to 99
Eu³⁺. Furthermore, the time-dependent luminescence of mixed 100
MOFs and the typical discrete visible emission bands of Eu 101
and Tb ions allowed for time-dependent bar-coding, whose 102
code evolution in the ms scale can easily be tuned by 103
controlling the Eu/Tb ratio. These advanced optical proper- 104
ties, combined with the demonstrated printability through 105
spray-coating, make these materials very promising as invisible 106
security inks for future anticounterfeiting technologies. 107

RESULTS AND DISCUSSION

Syntheses, Characterization, and Optical Stability of 108
Single-Ion Carborane-Based *mCB-Ln*. Colorless crystals of 109
 $[(Tb)_3(mCBL1)_4(NO_3)(DMF)_x] \cdot solv$ (*mCB-Eu*) and 110
 $[(Tb)_3(mCBL1)_4(NO_3)(DMF)_x] \cdot solv$ (*mCB-Tb*) were ob- 111
tained in high yields by solvothermal reactions in a mixture of 112
N,N-dimethylformamide (DMF)/methanol/H₂O at 95 °C for 113
114

115 48 h (see the [Experimental Section](#) for details and [Figure S1](#),
116 [Supporting Information](#)). Single-crystal X-ray diffraction
117 revealed that *mCB-Tb* crystallizes in the monoclinic *Pn*
118 space group, and the analysis of the structure revealed the
119 formation of a 3D framework based on the novel
120 [(Tb)₃(COO)₈(NO₃)(O_{DMF})₄] secondary building unit
121 (SBU) ([Figure 1](#) and [Table S1](#), [Supporting Information](#)).

122 The new SBU is composed of three nonequivalent
123 crystallographic terbium atoms, which are connected and
124 capped by bridging, chelate bridging or chelate *mCBL1*,
125 chelate NO₃⁻, and DMF molecules. Whereas, Tb(1) and
126 Tb(3) atoms ([Figure 1](#)) are eight-coordinated and Tb(2) is
127 seven-coordinated. As shown in [Figure 1](#), six *mCBL1* ligands
128 are coordinated to Tb(1) and those adopt two different
129 coordination modes (bridging and chelate bridging). The
130 coordination of Tb(1) is completed by a DMF molecule.
131 Tb(2) ([Figure 1](#)) shows, however, two coordinated DMF
132 molecules and five *mCBL1* ligands, all with bridging
133 coordination. Tb(3) shows a DMF molecule, a chelate
134 NO₃⁻, and five *mCBL1* ligands, the latter adopting bridging
135 coordination with the neighboring Ln atoms. Such coordina-
136 tion provides 1D-chains of Tb atoms, which are connected by
137 the *mCBL1* ligands and thus provide the observed 3D
138 structure ([Figure 1](#)). The varied coordination around the
139 three crystallographic-independent Ln atoms results in three
140 different Tb–Tb metal distances (Tb(1)–Tb(2) 5.5830(8),
141 Tb(2)–Tb(3) 5.2550(7), and Tb(1)–Tb(3) 4.6398(7) Å).
142 The Tb–O bond distances are in the range of 2.272(10)–
143 2.906(10) Å, all of which are comparable to related
144 compounds.^{83–86}

145 Fourier transform infrared (FTIR) spectroscopy ([Figure S2](#),
146 [Supporting Information](#)) and powder X-ray diffraction
147 (PXRD; [Figure S3](#), [Supporting Information](#)) analysis for
148 *mCB-Eu* and *mCB-Tb* compounds revealed that both are
149 isostructural and their experimental patterns match very well
150 with those simulated from the X-ray structure of *mCB-Tb*,
151 therefore, suggesting that the as-synthesized materials are pure
152 phases. Thermogravimetric (TGA; [Figure S4](#), [Supporting](#)
153 [Information](#)) and elemental analyses confirmed the chemical
154 composition of *mCB-Eu* and *mCB-Tb*. TGA curves for these
155 two materials revealed good thermal stabilities as the
156 frameworks are stable up to 400 °C.

157 As expected, both *mCB-Eu* and *mCB-Tb* showed very high
158 stability in neutral water and aqueous solutions of a broad
159 range of pH values (3–11) for at least 5 days. PXRD traces of
160 both, before and after incubation in water in a closed vial
161 perfectly match the simulated pattern derived from the single-
162 crystal structure of *mCB-Tb* ([Figure S5](#), [Supporting](#)
163 [Information](#)). In addition, optical images of the crystalline
164 samples after their immersion in water under the above-
165 mentioned conditions showed no significant morphology
166 change in the needle-like crystals nor evidence of surface
167 cracking ([Figure S5](#), [Supporting Information](#)). Such high
168 stability is ascribed to the presence of the carborane ligand.

169 The optical properties of the carborane-based *mCBL1* ligand
170 and the corresponding Eu³⁺ and Tb³⁺ compounds *mCB-Ln*
171 were investigated by collecting the ultraviolet–visible (UV–
172 vis) absorption and emission spectra of the compounds in the
173 solid state. The free ligand *mCBL1* exhibits a broad absorption
174 band around λ_{max} ~ 289 nm attributed to π → π* transitions
175 ([Figure S6](#), [Supporting Information](#)). The luminescence
176 spectrum for *mCBL1* shows a strong emission at λ_{em} = 312
177 nm (λ_{ex} = 280 nm) and an overall quantum yield (Φ) of 0.3%

([Figure S7](#), [Supporting Information](#)). The absorption spectra 178
of *mCB-Ln* display slight broadening of the UV bands. Upon 179
continuous-wave irradiation at λ_{ex} = 280 nm in an air 180
atmosphere and at room temperature, both *mCB-Eu* and 181
mCB-Tb solid crystals showed intense luminescence in the 182
visible region and sharp and well-resolved emission bands 183
([Figure 2](#)). The crystals' emissions were also observable by the 184

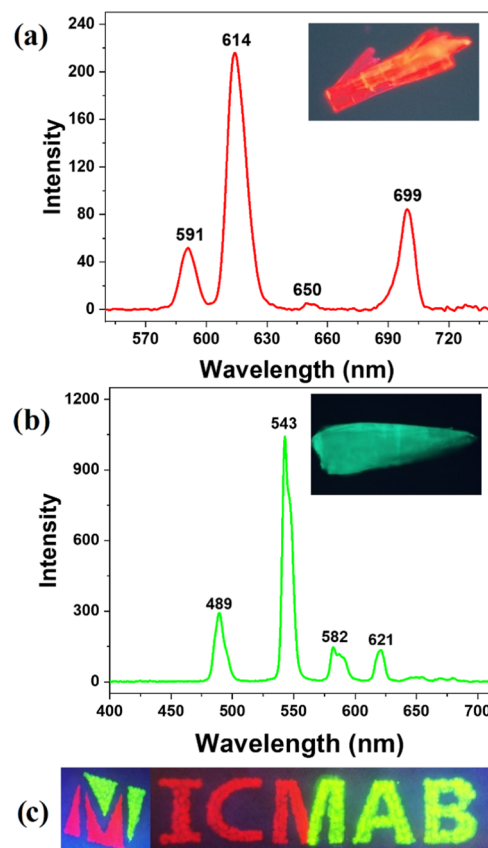


Figure 2. Solid-state emission spectra of *mCB-Eu* (a) and *mCB-Tb* (b) under continuous-wave irradiation (λ_{ex} = 280 nm) at room temperature. Insets: optical microscopy images of the corresponding crystals (λ_{exc} = 280 nm). (c) Photograph of the hand-painted logo of the Institut de Ciència de Materials de Barcelona (ICMAB) with *mCB-Eu* and *mCB-Tb* crystals (λ_{ex} = 254 nm).

naked eye, as shown in the insets of [Figure 2a,b](#). The 185
luminescence spectrum of *mCB-Eu* presented the typical 186
emission feature of Eu-based materials, with peaks at 591, 614, 187
650, and 699 nm, which correspond to characteristic 188
transitions of the Eu³⁺ ion: ⁵D₀ → ⁷F_J (J = 1, 2, 3, and 4),⁸⁷ 189
respectively, with the strongest being the ⁵D₀ → ⁷F₂ transition 190
at 614 nm ([Figure 2](#)). Overall, the *mCB-Eu* crystal yielded a 191
strong orange luminescence quantum yield (Φ = 20.5%), with a 192
1931 CIE color coordinate (0.62, 0.38). *mCB-Tb* showed 193
the typical luminescence of the Tb³⁺ ion, with emission peaks 194
at 489, 543, 582, and 620 nm, which are assigned to the ⁵D₄ → 195
⁷F_J (J = 6, 5, 4, and 3)⁸⁷ transitions of Tb³⁺ ions. The strongest 196
emission peak at 543 nm is associated with the ⁵D₄ → ⁷F₃ 197
transition ([Figure 2](#)). *mCB-Tb* presented a quite efficient 198
green emission (Φ = 49.8%) with the CIE color coordinate 199
(0.32, 0.58). These results clearly indicate that the carborane- 200
based *mCBL1* ligand is an excellent light-absorbing antenna 201
chromophore for sensitizing both ions (vide infra), and the 202
resulting MOFs presented quite high solid-state luminescence, 203

204 which is comparable to other Ln-MOFs ($\Phi_{\text{Eu-MOFs}} = 25\text{--}95$;
 205 $\Phi_{\text{Tb-MOFs}} = 7\text{--}75$).^{88–90} More importantly, the optical
 206 properties of *mCB-Eu* and *mCB-Tb* crystals did not suffer
 207 significant changes when these materials were suspended in
 208 water for 5 days or heated up to 180 °C for 24 h (Figure S8,
 209 Supporting Information), proving the high stability provided
 210 by the carborane ligand to the MOF optical properties. In fact,
 211 water suspensions of the *mCB-Eu* and *mCB-Tb* crystals could
 212 be successfully used to prepare two-colored patterned
 213 luminescence drawings (of ICMAB logo) through their
 214 deposition onto cellulose papers (Figure 2c and the
 215 Experimental Section), which did not affect the emission
 216 properties. Scanning electron microscopy (SEM) images
 217 corroborate the entrapment of microsize crystals between the
 218 fibers of the cellulose papers (Figure S9, Supporting
 219 Information), and steady-state luminescence spectra demon-
 220 strate that the crystals preserve their optical properties (Figure
 221 S10).

222 To analyze the mechanism of the luminescence process, the
 223 photochemical properties of the *mCBL1* have been explored
 224 using time-dependent density functional theory (TDDFT)
 225 methods (see the Computational Details section). The ligand
 226 antenna effect for the sensitization of the luminescence of the
 227 lanthanide compounds is known to be due to the transfer from
 228 a triplet state of the ligand to the first excited state of the
 229 lanthanide cation.^{14,16} Among others, the efficiency of the
 230 ligand as a sensitizer is related to the energy of its triplet state.
 231 The energy of the ⁵D₄ and ⁵D₀ first excited states for Tb³⁺ and
 232 Eu³⁺ cations for the studied system are 541 nm (18 464 cm⁻¹)
 233 and 614 nm (15 286 cm⁻¹). To have an efficient energy
 234 transfer from the sensitizer ligand to the lanthanide, previous
 235 studies¹⁴ have estimated that the energy of the triplet of the
 236 ligand should be at least 1850 cm⁻¹ above the lowest emitting
 237 excited states of the lanthanide. The first triplet state structure
 238 of the ligand has been optimized at the TDDFT level and
 239 resulted in a value of 20 449 cm⁻¹ for *mCBL1*, which perfectly
 240 fits with the requirement for an efficient energy transfer to both
 241 Tb³⁺ and Eu³⁺. The involved energies in the first singlet
 242 excitation and the triplet energy of *mCBL1* are represented in
 243 Figure 3 together with the involved orbitals. The first allowed
 244 excitation energies (calculated TDDFT values of 260 nm for
 245 the *mCBL1* ligand) are in agreement with those determined in
 246 the *mCBL1* ligand in a solid state around 251–289 nm (Figure

S6, Supporting Information). The analysis of the orbitals 247
 confirms that such transitions are mainly $\pi\text{--}\pi$ transitions with 248
 a large contribution from the phenyl rings. Both the calculated 249
 energies of the S₁ and T₁ states for *mCBL1* are significantly 250
 larger than those for some commonly used carbon-based 251
 chromophores.¹⁴ Thus, to understand the possible role of the 252
 carborane moiety in such unusually high energies of the first 253
 singlet excitation and triplet for our ligand, we have also 254
 explored the photophysical properties of the related ligand by 255
 substituting the carborane moiety with a phenyl ring 256
 ([1,1':3',1''-terphenyl]-4,4''-dicarboxylic acid, *mTDCA*) by 257
 TDDFT (Figures S11 and S12, Supporting Information). 258
 Consistent with the previous reports,¹⁴ both the calculated 259
 energies of the S₁ and T₁ states for *mTDCA* are significantly 260
 smaller than that for *mCBL1*. The comparison between the 261
 two ligands (Figures S11 and S12, Supporting Information) 262
 shows that the main difference is a symmetry breaking of the 263
 empty orbitals, probably due to the smaller symmetry of the 264
mCBL1 ligand for the central carborane. Whereas the *mCBL1* 265
 ligand structure remains almost unchanged in the S₁ and T₁ 266
 states, that for the *mTDCA* ligand shows that the noncoplanar 267
 ground-state structure results in a two-ring coplanar for the 268
 first triplet state (Figure S12, Supporting Information). This 269
 difference between the two ligands is reflected in the emission 270
 energies of the triplet (*mCBL1*, 20449 cm⁻¹; *mTDCA*, 16 474 271
 cm⁻¹). The orbitals involved in the emission are basically the 272
 lowest unoccupied molecular orbital (LUMO) and the highest 273
 occupied molecular orbital (HOMO) with a larger degree of 274
 localization in one part of the molecule in comparison with the 275
 singlet due to the decrease of symmetry (Figure 3). The 276
 unusually high energy for the triplet state for *mCBL1*, 277
 therefore, favored an effective energy transfer through 278
 nonradiated excited states of the metal until it reached the 279
 emissive levels and the metal-centered emission took place.¹⁴ 280
 Such energy transfer would be much less efficient in the case of 281
 the *mTDCA* ligand, which has no carborane, as the energy for 282
 its triplet state is of the order of that for Eu³⁺ and lower than 283
 that for Tb³⁺ (Figure S13, Supporting Information). 284

Synthesis, Characterization, and Optical Properties
 of Mixed-Ion Carborane-Based *mCB-Eu_yTb_{1-y}*. Currently, 285
 doping diverse Ln³⁺ ions into the same MOF has become an 286
 emerging method to accomplish stoichiometry-dependent 287
 color tunability.^{16,90,91} Due to the similar coordination 288
 environments, various Ln³⁺ ions can be introduced into the 289
 same MOF structure simultaneously. Energy transfer (ET) 291
 from one lanthanide to another lanthanide ion has also been 292
 observed to enhance the luminescence intensity in mixed- 293
 metal Ln-MOFs.^{88,91–96} For example, it has been reported that 294
 such ET between Tb and Eu ions induced up to 70% emission 295
 enhancement for the Tb-sensitized Eu emission in Ln-MOFs.⁸⁸ 296
 Thus, after once demonstrating the feasibility of using the 297
 hydrophobic carborane ligand to obtain water-stable MOFs 298
 with a high luminescence quantum yield, we aimed to 299
 investigate the possibility of obtaining other mixed Ln-MOFs 300
 (*mCB-Eu_yTb_{1-y}*) with variable amounts of each lanthanide, 301
 which are also expected to provide different luminescence 302
 colors. [(Eu_yTb_{1-y})₃(*mCBL1*)₄(NO₃)(DMF)_x]_n·*solv* (*mCB-* 303
Eu_yTb_{1-y}) were obtained as needle-like crystals (Figure S1, 304
 Supporting Information) and in good yields (>64%) by 305
 following the solvothermal procedure employed for the single- 306
 ion MOFs (see the Experimental Section for details). PXRD 307
 spectra for all *mCB-Eu_yTb_{1-y}* compounds match very well with 308
 the individual *mCB-Eu* and *mCB-Tb* counterparts and 309

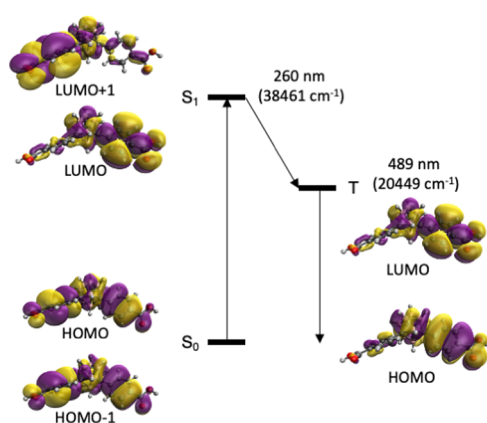


Figure 3. Energy diagram of the singlet and triplet states calculated using TDDFT with the B3LYP functional. The orbitals involved in such processes of the *mCBL1* ligand are shown.

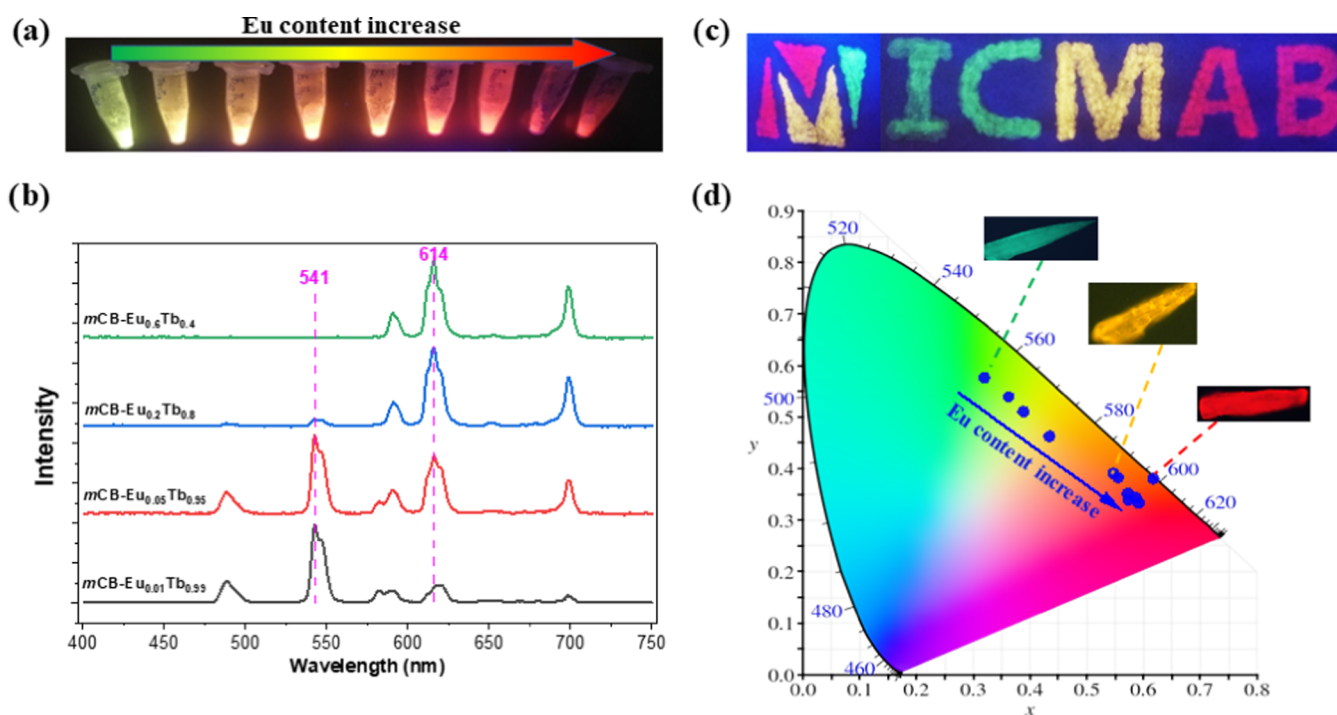


Figure 4. (a) Photographs of the powders of the mixed $mCB-Eu_yTb_{1-y}$ ($\lambda_{ex} = 254$ nm); (b) selection of steady-state emission spectra of the powders of mixed $mCB-Eu_yTb_{1-y}$ with various Eu/Tb molar ratios ($\lambda_{ex} = 280$ nm) (see Figure S14 for the spectra of all $mCB-Eu_yTb_{1-y}$ series); (c) photograph of the hand-painted logo of the Institut de Ciència de Materials de Barcelona (ICMAB) with $mCB-Tb$ (green), $mCB-Eu_{0.1}Tb_{0.9}$ (yellow), and $mCB-Eu$ (red) crystals; and (d) color coordinates drawn onto the 1931 CIE chromaticity diagram for the mixed $mCB-Eu_yTb_{1-y}$. Inset: luminescence microscopy images of the $mCB-Tb$ (green), $mCB-Eu_{0.1}Tb_{0.9}$ (yellow), and $mCB-Eu$ (red) crystals.

Table 1. CIE Color Coordinates, Luminescence Lifetimes, Energy Transfer Efficiencies, Absolute Quantum Yield, and Emission Ratio for $mCB-Eu$, $mCB-Tb$, and $mCB-Eu_yTb_{1-y}$ ($\lambda_{ex} = 280$ nm)

Ln	CIE color coordinates	τ (μs) ^a		$\eta_{Tb \rightarrow Eu}^b$ (%)	Φ (%)	emission ratio of Eu/Tb
		(⁵ D ₄ of Tb ³⁺)	(⁵ D ₀ of Eu ³⁺)			
Eu	(0.62, 0.38)		739.0		20.5 ± 1.3	1.000/0.000
Eu _{0.6} Tb _{0.4}	(0.59, 0.33)	23.2	749.7	97.3	41.2 ± 2.1	0.997/0.003
Eu _{0.5} Tb _{0.5}	(0.58, 0.34)	60.2	859.6	92.9	42.5 ± 1.4	0.974/0.026
Eu _{0.25} Tb _{0.75}	(0.59, 0.34)	117.9	934.1	86.1	47.8 ± 2.0	0.971/0.029
Eu _{0.2} Tb _{0.80}	(0.57, 0.35)	219.3	1023.9	74.2	58.1 ± 2.8	0.949/0.051
Eu _{0.1} Tb _{0.90}	(0.58, 0.38)	331.6	1079.6	61.0	69.2 ± 2.6	0.849/0.151
Eu _{0.08} Tb _{0.92}	(0.55, 0.39)	465.1	1084.1	45.3	63.6 ± 2.3	0.825/0.175
Eu _{0.05} Tb _{0.95}	(0.44, 0.46)	575.0	1153.8	32.3	56.4 ± 2.7	0.516/0.484
Eu _{0.03} Tb _{0.97}	(0.39, 0.51)	676.4	1367.3	20.4	55.7 ± 1.7	0.248/0.752
Eu _{0.01} Tb _{0.99}	(0.36, 0.54)	818.3	1714.9	3.7	52.6 ± 2.5	0.230/0.770
Tb	(0.32, 0.58)	849.7			49.8 ± 1.8	0.000/1.000

^aDecay curves for mixed Ln-MOFs were fitted by a biexponential function ($I = A_1 \exp(-t/\tau_1) + A_2 \exp(-t/\tau_2)$), and the average lifetime was calculated from the equation of $\tau = (A_1\tau_1^2 + A_2\tau_2^2)/(A_1\tau_1 + A_2\tau_2)$.^{22,97} ^bEnergy transfer efficiency was determined by the function of $\eta_{Tb \rightarrow Eu} = 1 - \tau/\tau^0$.⁹⁶

310 therefore also proved to be also isostructural (Figure S3). The
311 Eu/Tb molar ratios in the mixed MOFs were determined by
312 inductively coupled plasma (ICP) measurements, revealing
313 that the ratios match reasonably well with the original molar
314 ratios of Eu^{3+}/Tb^{3+} during the syntheses (Table S2).

315 Steady-state irradiation ($\lambda_{ex} = 280$ nm) of the obtained solid
316 $mCB-Eu_yTb_{1-y}$ crystal powders yielded strong emission in the
317 visible spectral region in all cases, with the emitted color finely
318 and fully tunable between the two extreme colors (green and
319 red) of the single-element Ln-MOFs (Figure 4a).

320 A detailed analysis of the luminescence data for $mCB-$
321 Eu_yTb_{1-y} crystals (Table 1, Figures 4b and S14, Supporting
322 Information) discloses some interesting results. On the one

hand, the increase in the molar fraction of Eu from 0 to 0.08 in
the mixed Ln-MOF preparation caused a quite significant and
gradual shift of the emission color, from green ($mCB-Tb$) to
orange (Figure 4b), as shown also by the corresponding CIE
color coordinates and representative luminescence microscopy
images (inset Figure 4d). However, a further increase of the Eu
percentage (up to 100%) yielded less variation in the emission
ratios of the two elements in $mCB-Eu_yTb_{1-y}$ and thus a less
significant color change toward the red region of $mCB-Eu$.
This was ascribed to the negligible Tb emission contribution in
the $mCB-Eu_yTb_{1-y}$ crystals above a threshold Eu amount
(10%), as a consequence of an efficient Tb^{3+} energy transfer to
 Eu^{3+} (Table 1).

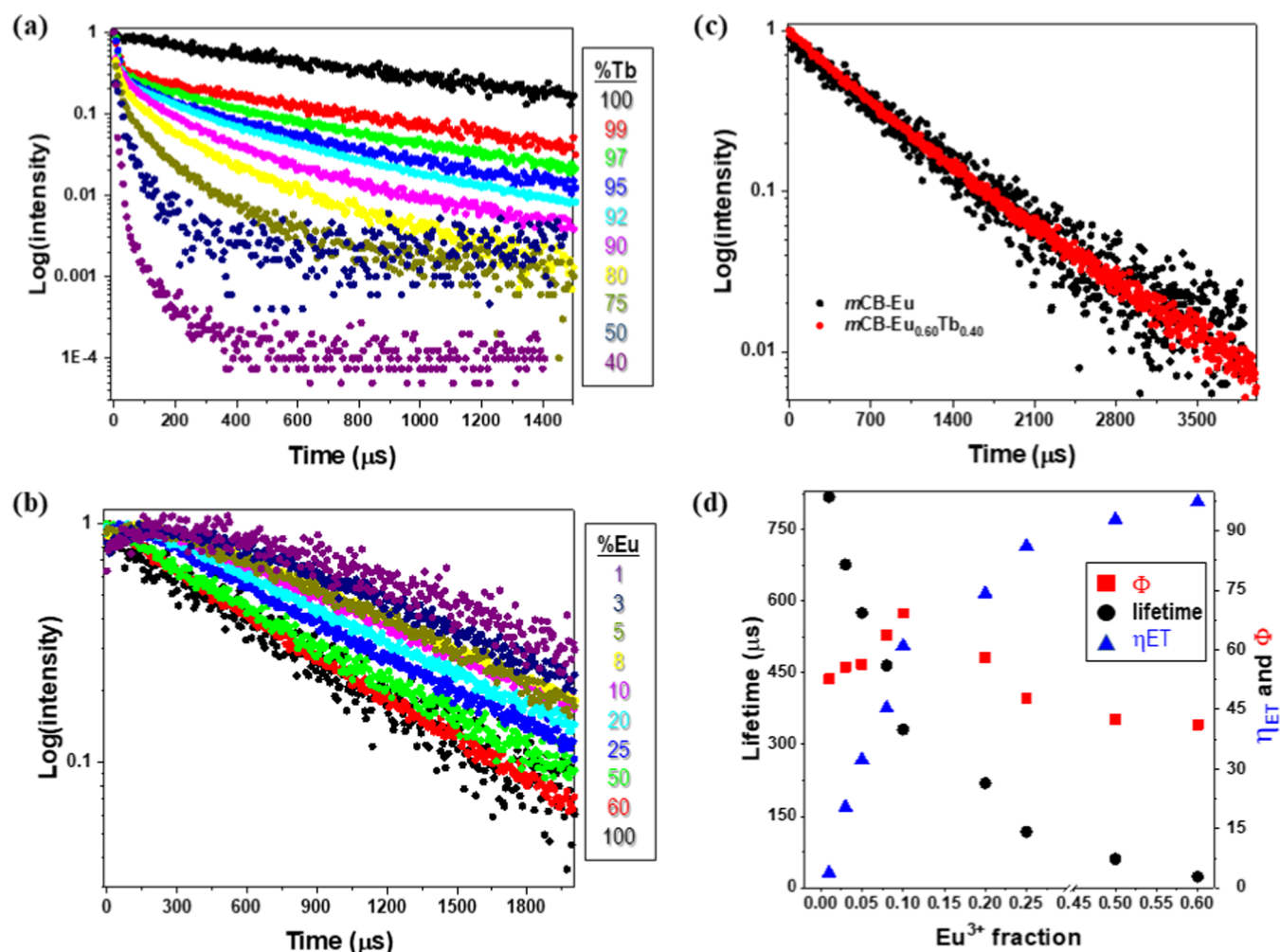


Figure 5. (a) Luminescence decays of Tb ($\lambda_{em} = 541$ nm) in the different MOFs ($\lambda_{exc} = 280$ nm); (b) luminescence decays of Eu ($\lambda_{em} = 614$ nm) in the different MOFs ($\lambda_{exc} = 280$ nm); (c) comparison of the luminescence decay of $mCB-Eu_{0.60}Tb_{0.40}$ with $mCB-Eu$; and (d) average lifetimes, ET quantum yield, and luminescence quantum yield trends against the Eu^{3+} fraction.

336 These results indicate that the tunable emission in the $mCB-$
 337 Eu_yTb_{1-y} crystals is not only related to the additive relative
 338 luminescence of the Eu^{3+} and Tb^{3+} component elements but is
 339 also the result of efficient energy transfer processes from Tb^{3+}
 340 to Eu^{3+} ,^{88,91–96,98} which results in an enhancement of the of
 341 Eu^{3+} luminescence instead of additive emissions from each ion.
 342 These mixed-ion MOF crystals were successfully employed to
 343 prepare multicolored MOF patterned luminescence drawings via
 344 hand-painting onto cellulose papers, which are colorless (i.e.,
 345 invisible crystals) under ambient light, while preserving the
 346 emission properties under UV radiation, making them highly
 347 suitable for anticounterfeiting technologies (Figure 4c).
 348 Further evidence of the Tb-Eu ET process is derived from
 349 the study of the luminescence decays of Tb^{3+} and Eu^{3+} ions in
 350 all of the above compounds, registered at $\lambda_{em} = 541$ ($^5D_4 \rightarrow$
 351 7F_5 of Tb^{3+}) and 614 nm ($^5D_0 \rightarrow ^7F_2$ of Eu^{3+}), respectively,
 352 upon pulsed light irradiation at $\lambda_{exc} = 280$ nm (Figures 5 and
 353 S15–26, Supporting Information).

354 The luminescence decay curves of $mCB-Tb$ and $mCB-Eu$
 355 exhibited the typical monoexponential decay functions with
 356 calculated lifetimes of 849.7 and 739.0 μs , respectively, which
 357 are similar to those reported for other Eu- and Tb-based
 358 compounds (Table 1 and Figure S15, Supporting Informa-
 359 tion).⁹⁰ The emission decay curves of Tb^{3+} in $mCB-Eu_yTb_{1-y}$,

360 changed to biexponential decay functions, with increasingly
 361 shorter average decay times (Table 1 and Figures 5a and S16,
 362 Supporting Information). In contrast, in the emission curve of
 363 Eu^{3+} of the mixed-metal MOFs, a signal increase at shorter
 364 times is followed by a luminescence decrease. The increasing
 365 signal is slow for $mCB-Eu_{0.01}Tb_{0.99}$, but becomes shorter (i.e.,
 366 faster) as the Eu^{3+} concentration increases, in good agreement
 367 with the lifetime decrease of the Tb^{3+} (Figures 5b and S17).
 368 The apparent increase of Eu^{3+} lifetimes at smaller
 369 concentrations is the result of the convolution of the Eu^{3+} formation
 370 and its luminescence decay. In $mCB-Eu_{0.6}Tb_{0.4}$, the signal rise
 371 is so fast that the measured decay matches with the
 372 monoexponential decay function and lifetime of the pure
 373 Eu^{3+} MOF (Figure 5c). These results corroborate the ET
 374 process between the Tb^{3+} and Eu^{3+} , which becomes more
 375 efficient as the concentration of Eu^{3+} increases, becoming
 376 nearly quantitative (97.3%) in $mCB-Eu_{0.6}Tb_{0.4}$ (Figure 5c).

377 Remarkably, the absolute quantum yields for $mCB-Eu_yTb_{1-y}$
 378 did not follow the same trend and varied greatly within these
 379 mixed-metal MOFs: it increased passing from the values of the
 380 single-ion crystals $mCB-Tb$ (49.8%) and $mCB-Eu$ (20.5%) up
 381 to a maximum of 69.2% in $mCB-Eu_{0.1}Tb_{0.90}$ (Table 1 and
 382 Figure 5d), which represents an outstanding increase of 237%
 383 of the quantum yield of that for $mCB-Eu$ (20.5%) or an

384 increase of 39% with respect to that for *mCB-Tb* (49.8%).
 385 Such a huge enhancement of the overall quantum yield reveals
 386 that the ligand-to-Tb³⁺ and Tb³⁺-to-Eu³⁺ consecutive energy
 387 transfers are much more efficient than the direct ligand-to-Eu³⁺
 388 energy transfer. However, when the Eu³⁺ amount increases
 389 significantly (20%), it starts competing with Tb³⁺ in the ET
 390 transfer from the ligand, lowering the overall quantum yield
 391 (Figure 6). The observed energy transfer process is well known
 392 to happen within these two metals, although such an increase
 393 in the quantum yield has not been reported.

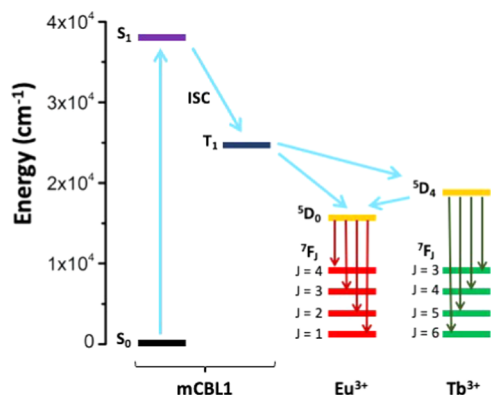


Figure 6. Schematic diagram of the energy absorption to the singlet state (S_0) of the *mCBL1* ligand, transfer to the triplet state (T_1), energy transfer, and emission processes of *mCB-Eu_yTb_{1-y}*.

394 **Time-Dependent Optical Properties of *mCB-Eu_yTb_{1-y}***
 395 **Crystals for Anticounterfeiting.** A precise tailoring of a
 396 lifetime at an emission band can entail a virtually unlimited
 397 number of unique temporal codes.⁹⁹ However, to date, a few
 398 reports have considered Ln-MOFs for lifetime-based encoding
 399 in the visible range for optical multiplexing,^{27,98,100} but tunable
 400 fluorescent lifetime has not been proposed for anticounterfeit-
 401 ing. The energy transfer process between Eu³⁺ and Tb³⁺ ions
 402 and the control of their decay rates in different *mCB-Eu_yTb_{1-y}*
 403 crystals allowed us to explore two optical features of interest
 404 for anticounterfeiting technologies for the first time: time-
 405 dependent emission color change and time-dependent bar-
 406 coding. These were demonstrated for *mCB-Eu_{0.01}Tb_{0.99}*, *mCB-*
 407 *Eu_{0.1}Tb_{0.90}*, and *mCB-Eu_{0.60}Tb_{0.40}* crystals where the lumines-
 408 cence lifetime variation of Eu³⁺ and Tb³⁺ is achieved by
 409 changing the metal stoichiometry in *mCB-Eu_yTb_{1-y}*.

410 **Time-Dependent Emission Spectra (and Color).** These
 411 were recorded at various delay times (0.5–10 000 μ s) upon
 412 irradiation with a 266 nm pulsed neodymium-doped yttrium
 413 aluminum garnet (Nd-YAG) laser (Figure 7a–f). The spectra
 414 measured for the *mCB-Eu_{0.1}Tb_{0.90}* crystals gradually changed
 415 from green (0.40, 0.56) to red (0.61, 0.37) (Figure 7b),
 416 following a similar color variation trend registered under
 417 continuous-wave irradiation for MOFs made of different ion
 418 compositions. In this case, different colors were obtained from
 419 a single MOF at different delay times. The green color
 420 observed at shorter delays was due to the Tb³⁺ emission, which
 421 was still not quenched efficiently by Eu³⁺. The red color
 422 recorded at longer delays was ascribed to the Eu³⁺ emission
 423 after Tb³⁺ was fully quenched (complete ET). The
 424 intermediate colors were the result of the contribution of
 425 both the sensitized Eu³⁺ and the still not quenched Tb³⁺. When
 426 the same study was carried out for the *mCB-Eu_{0.01}Tb_{0.99}*
 427 powder, time-dependent emission spectra were still recorded,

though they yielded greener coordinates at shorter delay times 428
 (0.33, 0.60) and a yellow color at longer delays (0.42, 0.52). 429
 The different range of color variation for this compound was 430
 ascribed to the slower Tb³⁺–Eu³⁺ energy transfer process that 431
 delays the loss of the green emission of Tb³⁺, which thus 432
 contributes significantly to the overall spectra until the end of 433
 the luminescence (Figure 7a). The opposite effect was 434
 observed for the *mCB-Eu_{0.60}Tb_{0.40}* crystals, which showed 435
 time-dependent emission spectra changing from yellow (0.49, 436
 0.49) to red (0.59, 0.36), as shown in Figure 7c. In this case, by 437
 the time the first spectrum is recorded, the emission 438
 contribution of Tb³⁺ is already partially merged with the 439
 sensitized Eu³⁺ emission, providing the yellow coloring. 440
 Moreover, Tb³⁺ emission is, in this case, quickly quenched, 441
 yielding delayed emission spectra with only the red 442
 contribution of Eu³⁺. Therefore, these materials not only 443
 show time-dependent emission spectra and color coordinates 444
 but also enable the emission color range to be changed (and 445
 the starting and ending point) by simply modifying the 446
 stoichiometry of the ions. This time-dependent color change, 447
 observed in all mixed *mCB-Eu_yTb_{1-y}*, introduces more 448
 complexity to the luminescence color tunability through the 449
 relative proportion of Eu³⁺/Tb³⁺. 450

451 **Time-Dependent Bar-Coding.** For the second feature, we
 452 explored the possibility of using the discrete and narrow
 453 emission bands of lanthanide ions to obtain time-dependent
 454 bar-coding. For this, we performed pulsed measurements of
 455 the three compounds above, recording the projection of the
 456 emitted photons over time onto the detecting matrix of a
 457 charge-coupled device (CCD) camera. Taking advantage of
 458 the different decay profiles and rates of Tb³⁺ (emission
 459 decrease after the pulse) and Eu³⁺ (increase and then
 460 decrease), luminescent bar-coding changing the number and
 461 relative intensities of the lines (associated with the emitted
 462 bands of the two ions) was obtained (Figures 7g–i and S27–
 463 S29, Supporting Information). It is easy to understand the
 464 relevance of this time-dependent bar-coding to create dynamic
 465 security messages and labels changing the provided informa-
 466 tion in a microsecond–millisecond time scale. For *mCB-*
 467 *Eu_{0.1}Tb_{0.90}*, the initial and final bar-code lines are related to
 468 the emission bands of nearly pure Tb³⁺ or Eu³⁺, respectively
 469 (Figures 7h and S28, Supporting Information). This means
 470 that the coded information changes all of the time along the
 471 recorded time frame. In the case of *mCB-Eu_{0.01}Tb_{0.99}* (slower
 472 ET), the emission of Eu³⁺ only starts appearing after 500 μ s,
 473 which means the coded information only starts changing at
 474 later delays (Figures 7g and S27, Supporting Information).
 475 Finally, for the *mCB-Eu_{0.60}Tb_{0.40}* powder (fast ET), the Tb³⁺
 476 lines only slightly appear for the first few microseconds, which
 477 means the coding information will not change further after a
 478 short delay time (Figures 7i and S29, Supporting Information).
 479 Similar results were obtained on irradiating with lower-energy
 480 excitation wavelengths (355 nm, Figures S30 and S32,
 481 Supporting Information).

482 These very promising results pushed us to use these
 483 encoding materials for printing onto cellulose papers to
 484 simultaneously obtain time-dependent luminescent colors
 485 and codes onto patterned spatial domains, which will bring
 486 new schemes for advanced anticounterfeiting technologies and
 487 security data storage. Printing was carried out through a
 488 custom-made spray-coating technique in which a prefabricated
 489 mask with a logo was layered onto the substrate under the
 490 nozzle (Figure S33, Supporting Information). The printed

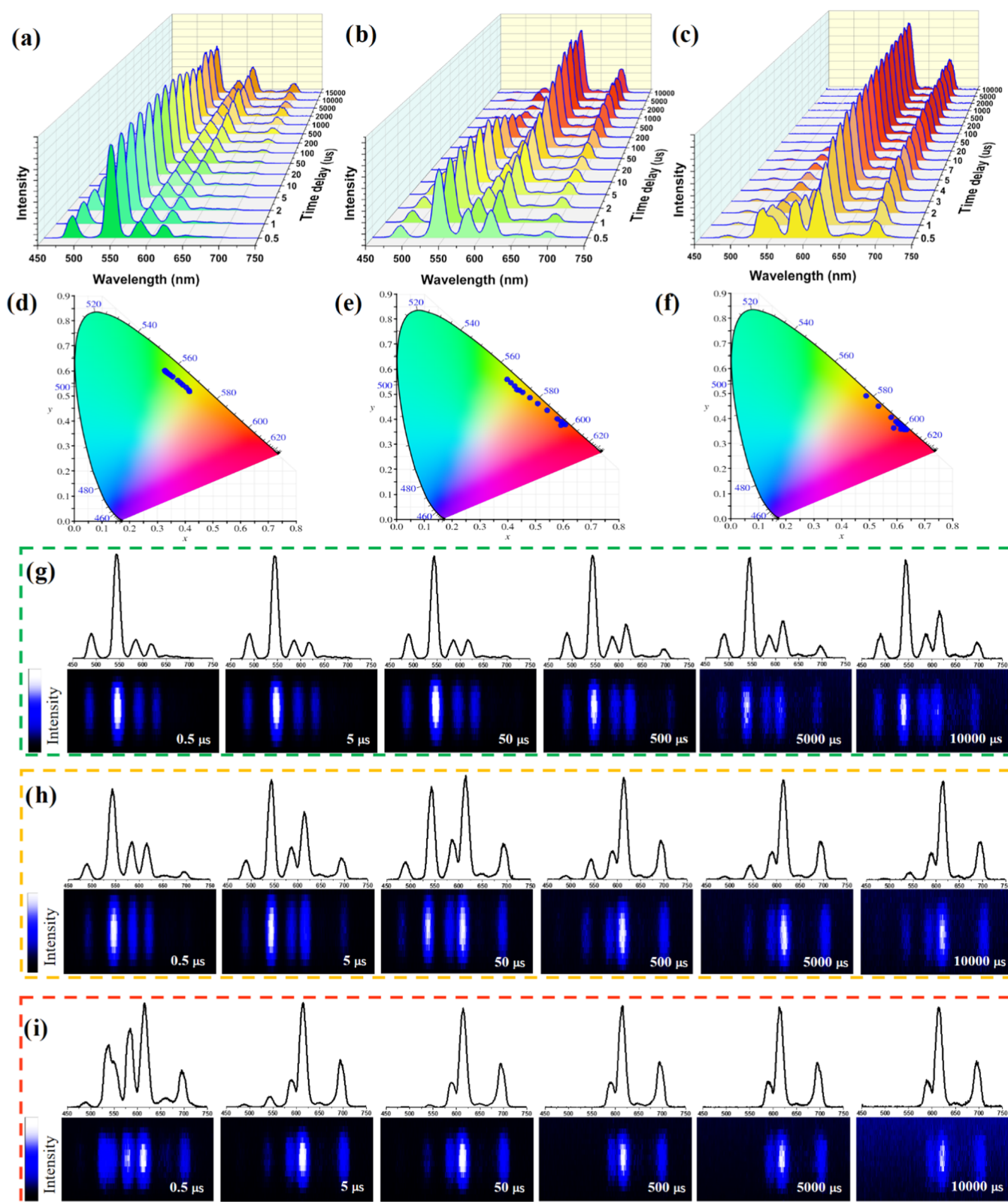


Figure 7. Time-dependent emission spectra of (a) $m\text{CB-Eu}_{0.01}\text{Tb}_{0.99}$, (b) $m\text{CB-Eu}_{0.1}\text{Tb}_{0.9}$, and (c) $m\text{CB-Eu}_{0.6}\text{Tb}_{0.4}$ powders at various time delays and (d–f) corresponding CIE coordinates ($\lambda_{\text{ex}} = 266 \text{ nm}$). Time-dependent bar codes of (g) $m\text{CB-Eu}_{0.01}\text{Tb}_{0.99}$, (h) $m\text{CB-Eu}_{0.1}\text{Tb}_{0.9}$, and (i) $m\text{CB-Eu}_{0.6}\text{Tb}_{0.4}$ ($\lambda_{\text{ex}} = 355 \text{ nm}$).

491 colorless cellulose paper showed no patterns under daylight
 492 while preserving the emission properties under UV radiation.
 493 Under continuous-wave UV irradiation, the printed pattern can
 494 be recognized (Figure 8a). The recorded steady-state emission

spectra (Figure S34) yielded an orange color with coordinates 495
 at (0.57, 0.38) in the CIE 1931 color space diagram as the 496
 crystal powder (Figure 4b). However, measurements under 497
 pulsed irradiation (266 nm) revealed time-dependent 498

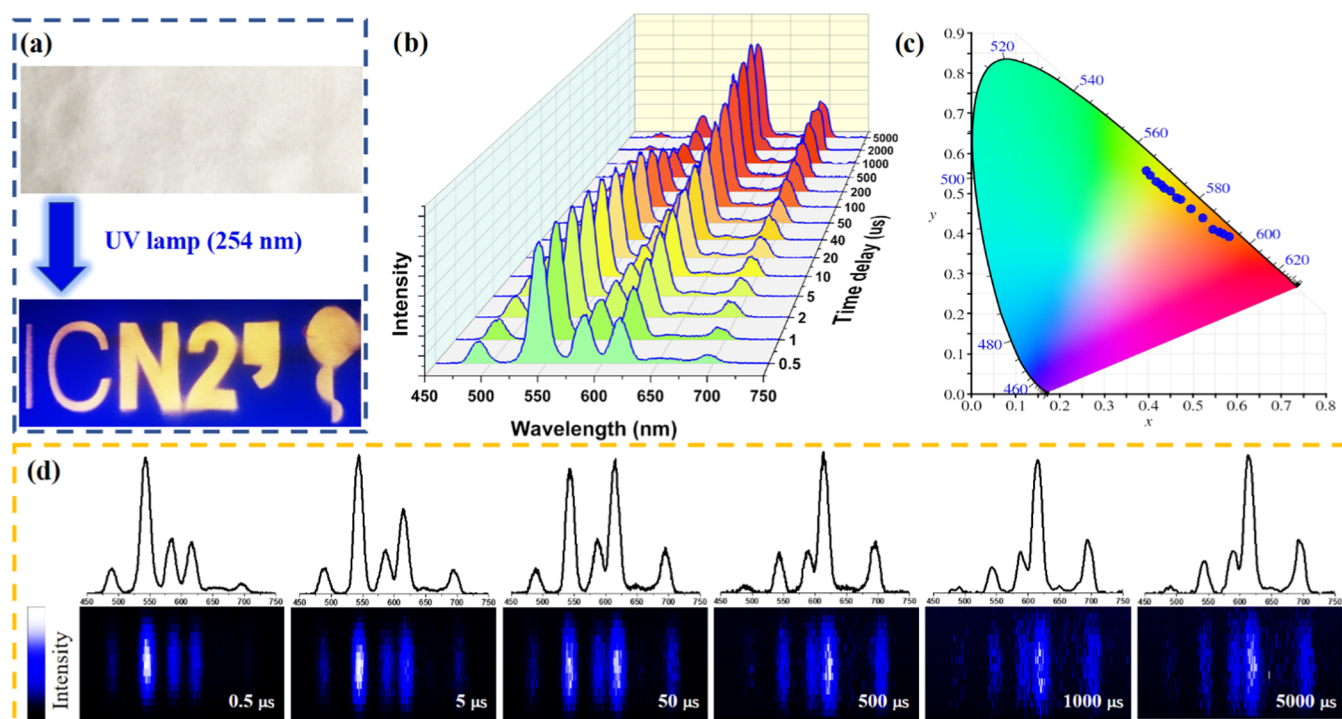


Figure 8. (a) Spray-coated $mCB-Eu_{0.01}Tb_{0.99}$ using a prepatterned mask to illustrate the logo on Institut de Nanociencia i Nanotecnologia, (b) time-dependent emission spectra of the printed $mCB-Eu_{0.01}Tb_{0.99}$, (c) corresponding color coordinates in the 1931 CIE diagram, and (d) time-dependent bar codes of the printed $mCB-Eu_{0.01}Tb_{0.99}$ ($\lambda_{ex} = 355$ nm).

499 luminescent spectra (Figure 8b), color (Figure 8c), and bar
500 codes (Figures 8d and S31), confirming that the optical
501 properties of the powder are preserved after printing in
502 cellulose papers, the substrate most used for sensitive
503 documents.

504 ■ CONCLUSIONS

505 Herein, we report carborane ligand-based Ln-MOFs (also
506 known as lanthanide coordination polymers [Ln-CPs]) as a
507 novel class of water- and temperature-stable materials that
508 exhibit multimodal luminescence tunability. We have synthe-
509 sized and fully characterized a new family of isostructural
510 $mCB-Eu_yTb_{1-y}$ ($y = 0-1$) luminescence MOFs built on a
511 highly hydrophobic carborane linker ($mCBL1$). Ln-MOFs
512 prepared from Eu^{3+} and Tb^{3+} at different ratios permitted easy
513 modulation of the luminescence from the green to the red
514 region of the 1931 CIE lab space diagram. This color tunability
515 was ascribed to the controlled energy transfer (ET) efficiency
516 between Tb^{3+} and Eu^{3+} . The ET process was corroborated by
517 both spectral measurements and lifetime decays, which showed
518 nearly quantitative ET efficiency when the Eu^{3+} was increased
519 to 60%. The different lifetimes of Tb^{3+} and Eu^{3+} in each MOF
520 also allowed time-dependent spectral changes in the ms time
521 scale to be obtained. An outstanding increase of 237% of the
522 quantum yield of $mCB-Eu$ (20.5%) in the mixed $mCB-$
523 $Eu_{0.1}Tb_{0.9}$ (69.2%) is achieved, along with an increased and
524 tunable lifetime luminescence (from about 10 to 400 μs), all of
525 these promoted by a highly effective ET process. Moreover,
526 taking advantage of the narrow bands of Ln, we were able to
527 obtain time-dependent bar codings, whose bars and the rate of
528 change could be modulated by the MOF composition.

529 These results, together with the fact that these particles
530 could be printed through spray-coating, make these materials

highly attractive for dynamic color-changing security inks in 531
532 anticounterfeiting technologies.

533 ■ EXPERIMENTAL SECTION

534 All chemicals were of reagent-grade quality. They were purchased
535 from commercial sources and used as received. A 1,7-di(4-
536 carboxyphenyl)-1,7-dicarba-*closa*-dodecaborane ligand ($mCBH_2L1$)
537 was synthesized according to the literature procedure.¹⁰¹

**Synthesis of $\{[(Ln)_3(mCBL1)_4(NO_3)(DMF)_n] \cdot Solv\}$ ($mCB-Ln$,
538 Where Ln = Eu, Tb, and Eu_xTb_{1-x}).** The $mCB-Ln$ materials were
539 prepared by solvothermal synthesis. In a typical preparation,
540 $mCBH_2L1$ (0.03 mmol) and $Ln(NO_3)_3$ (0.02 mmol; Ln = Eu, Ln)
541 were added to a mixture of DMF (0.5 mL)/methanol (1.5 mL)/ H_2O
542 (0.3 mL) and sonicated until complete dissolution of all reagents. The
543 above mixture was transferred to an 8 dram vial and heated at 95 °C
544 in an oven for 48 h. Needle-like white crystals were collected and
545 washed with DMF (yield based on the lanthanides: 71% for $mCB-Tb$
546 and 64% for $mCB-Eu$). IR (ATR; selected bands; cm^{-1}): 2601 (BH);
547 1658 (C=O from DMF); and 1590 (C=O from carboxylate).
548 Elemental analysis (%) calculated for $[Eu_3(mCB-L)_4(NO_3)(DMF)_2] \cdot$
549 $6H_2O$: C 36.23, H 4.14, N 2.07; found: C 36.36, H, 4.24, N 1.82.
550 Elemental analysis (%) calculated for $[Tb_3(mCB-L)_4(NO_3)(DMF)_2] \cdot$
551 $6H_2O$: C 36.23, H 4.14, N 2.07; found: C 36.16, H, 4.31, N 1.66.
552

The mixed $mCB-Eu_xTb_{1-x}$ materials were prepared using the same
553 method by adjusting the ratios of $Eu(NO_3)_3/Tb(NO_3)_3$ salts.
554

Preparation of the Multimodal Anticounterfeiting Model.
555 Anticounterfeiting tags were painted using fluorescent inks with an
556 optimized concentration of Ln-MOFs (0.2 mg/mL). To prepare the
557 aqueous security inks, crystals of Ln-MOFs were manually ground and
558 then dispersed in water with the help of ultrasonication. A
559 commercially available filter paper was used as a substrate in this
560 study. A handwritten image was obtained using a stick contaminated
561 with the security inks. To get a more regular printing pattern, a
562 custom-made spray-coating technique was employed, in which a
563 prefabricated mask with a logo was layered onto the substrate under
564 the nozzle (Figure S31). It should be mentioned that the 565
566 luminescence intensity of the inks and the subsequently printed

567 patterns could be easily adjusted by varying the concentration of Ln-
568 MOFs.

569 **Instruments and Characterization.** A crystal suitable for single-
570 crystal X-ray diffraction (SCXRD) with dimensions $0.18 \times 0.07 \times$
571 0.04 mm^3 was selected and mounted on a MITIGEN holder with
572 silicon oil on a ROD, Synergy Custom system, HyPix diffractometer.
573 The crystal was kept at a steady $T = 100(2) \text{ K}$ during data collection.
574 The structure was solved with the ShelXT 2014/5¹⁰² solution
575 program using dual methods and using Olex2 1.5- α ¹⁰³ as the graphical
576 interface. The model was refined with ShelXL 2016/6¹⁰⁴ using full-
577 matrix least-squares minimization on F^2 . The structure is refined in
578 the monoclinic space-group Pn with a β angle of $90.094(1)^\circ$ and a
579 twin law replicating orthorhombic symmetry $(100, 0\bar{1}0, 00\bar{1})$, $BASF =$
580 0.43 . The DMF molecules were refined as rigid groups with various
581 thermal parameter restraints. Attenuated total reflection Fourier
582 transform infrared (ATR-FTIR) spectra were recorded using a
583 PerkinElmer Spectrum One spectrometer equipped with a Universal
584 ATR sampling accessory. Spectra were collected with a 2 cm^{-1}
585 spectral resolution in the $4000\text{--}650 \text{ cm}^{-1}$ range. Elemental analyses
586 were obtained using a Thermo (Carlo Erba) Flash 2000 Elemental
587 Analyzer, configured for wt % CHN. Thermogravimetric analysis
588 (TGA) was performed in N_2 , on an nSTA 449 F1 Jupiter instrument
589 (heating rate: $10 \text{ }^\circ\text{C}/\text{min}$; temperature range: $25\text{--}800 \text{ }^\circ\text{C}$). Powder
590 X-ray diffraction (PXRD) was recorded at room temperature on a
591 Siemens D-5000 diffractometer with $\text{Cu K}\alpha$ radiation ($\lambda = 1.5418 \text{ \AA}$,
592 35 kV , 35 mA , increment $= 0.02^\circ$). Inductively coupled plasma-mass
593 spectrometry (ICP-MS) measurements were carried out on an Agilent
594 ICP-MS 7700x apparatus. Scanning electron microscopy (SEM)
595 (QUANTA FEI 200 FEGESEM) and optical microscopy (Olympus
596 BX52) were used to monitor the morphology and color changes at
597 various conditions. Solid-state UV–visible spectra were obtained on a
598 UV–Vis–NIR V-780 spectrophotometer equipped with an opera-
599 tional range of $200\text{--}1600 \text{ nm}$.

600 Emission spectra were obtained with a PTI Quantamaster 300
601 fluorimeter, putting the solid powder in a custom-made holder and
602 setting the holder plane at 45° with the direction of the incident light
603 and the optical path toward the detector. All spectra were obtained on
604 irradiating with a continuous-wave Xe lamp at $\lambda_{\text{exc}} = 280 \text{ nm}$. Lifetime
605 measurements were obtained with the same fluorimeter, but at an
606 excitation of 280 nm with a pulsed Xe lamp (100 Hz , $2 \mu\text{s}$ integration
607 time). Absolute luminescence quantum yields (Φ) of solid-state
608 samples under continuous-wave excitation ($\lambda_{\text{ex}} = 280 \text{ nm}$) were
609 determined using the quantum yield fluorimeter Hamamatsu C9920-
610 02G, equipped with an integrating sphere, connected to the lamp with
611 an optical fiber, at room temperature in the air. Φ values were
612 calculated based on the number of photons absorbed and emitted by
613 the sample. A detailed measurement procedure can be found in a
614 previous report.⁹⁷ Reported overall Φ values are averages of at least
615 three independent determinations.

616 Delay time-dependent emission spectra and bar codes under a
617 pulsed excitation ($\lambda_{\text{ex}} = 355$ and 266 nm) were recorded irradiating
618 with the fourth and third harmonic of a Nd:YAG (Brilliant B, Spectra
619 Physics) ns pulsed laser. The emission was recorded using an Andor
620 ICCD camera coupled to a spectrograph, setting the sample powder
621 or loaded cellulose papers at 45° with the incident beam and the
622 optical path toward the detector. Measurements were recorded at a 1
623 Hz frequency, 100 ns (266 nm) or 5000 ns (355 nm) integration
624 time, and applying different delays with respect to the excitation pulse.

625 **Computational Details.** To analyze the photochemical properties
626 of the mCB ligand, computational methods have been employed. The
627 calculations were performed using the Gaussian 16 program⁸⁴ with
628 the TDDFT method and the exchange–correlation functional
629 B3LYP.⁸⁵ Other functionals commonly employed in the TDDFT
630 calculation of organic systems were tested (PBE0,⁸⁶ LC-wPBE⁸⁷).
631 However, due to the larger exact exchange contributions, they provide
632 a more energetic transition than B3LYP and consequently, poorer
633 agreement with the experimental data. The 6-311G* basis set was
634 employed for the geometry optimization and the 6-311+G** basis set
635 for the TDDFT calculations. Neutral molecules including the acidic

hydrogen atoms were included because they provide a better 636
description of the metal-coordinated ligands than the anionic ligands. 637

■ ASSOCIATED CONTENT 638

Supporting Information 639

The Supporting Information is available free of charge at 640
<https://pubs.acs.org/doi/10.1021/acs.chemmater.2c00323>. 641

Optical and SEM images, IR, TGA, crystallographic 642
data, powder X-ray diffraction, UV–vis spectra, 643
luminescence spectra and decay curves, TDDFT results, 644
and time-dependent emission spectra (PDF) 645

■ AUTHOR INFORMATION 646

Corresponding Authors 647

Claudio Roscini – Catalan Institute of Nanoscience and 648
Nanotechnology (ICN2), CSIC, and The Barcelona Institute 649
of Science and Technology (BIST), Bellaterra, Barcelona 650
08193, Spain; orcid.org/0000-0002-0157-8934;
Email: claudio.roscini@icn2.cat 652

José Giner Planas – Institut de Ciència de Materials de 653
Barcelona (ICMAB-CSIC), 08193 Bellaterra, Spain;
orcid.org/0000-0002-1648-2169; Email: jginerplanas@icmab.es 655
656

Authors 657

Zhen Li – Institut de Ciència de Materials de Barcelona 658
(ICMAB-CSIC), 08193 Bellaterra, Spain 659

Rosario Núñez – Institut de Ciència de Materials de 660
Barcelona (ICMAB-CSIC), 08193 Bellaterra, Spain;
orcid.org/0000-0003-4582-5148 662

Mark E. Light – Department of Chemistry, University of 663
Southampton, Highfield, Southampton SO17 1BJ, U.K. 664

Eliseo Ruiz – Departament de Química Inorgànica i Orgànica 665
and Institut de Recerca de Química Teòrica i Computacional, 666
Universitat de Barcelona, 08028 Barcelona, Spain;
orcid.org/0000-0001-9097-8499 668

Francesc Teixidor – Institut de Ciència de Materials de 669
Barcelona (ICMAB-CSIC), 08193 Bellaterra, Spain;
orcid.org/0000-0002-3010-2417 671

Clara Viñas – Institut de Ciència de Materials de Barcelona 672
(ICMAB-CSIC), 08193 Bellaterra, Spain; [orcid.org/](https://orcid.org/0000-0001-5000-0277)
[0000-0001-5000-0277](https://orcid.org/0000-0001-5000-0277) 674

Daniel Ruiz-Molina – Catalan Institute of Nanoscience and 675
Nanotechnology (ICN2), CSIC, and The Barcelona Institute 676
of Science and Technology (BIST), Bellaterra, Barcelona 677
08193, Spain; orcid.org/0000-0002-6844-8421 678

Complete contact information is available at: 679
<https://pubs.acs.org/10.1021/acs.chemmater.2c00323> 680

Author Contributions 681

This manuscript was written through contributions of all 682
authors. All authors have given approval to the final version of 683
the manuscript. 684

Notes 685

The authors declare no competing financial interest. 686

■ ACKNOWLEDGMENTS 687

This work was financially supported by the MINECO 688
(PID2019-106832RB-I00), MICINN through the Severo 689
Ochoa Program for Centers of Excellence for the FUNFU- 690
TURE (CEX2019-000917-S, MDM-2017-0767, and SEV- 691
2017-0706 projects), grant RTI2018-098027-B-C21 funded 692

693 by MCIN/AEI/10.13039/501100011033 and by ERDF A way
694 of making Europe and the Generalitat de Catalunya (2017/
695 SGR/1720 and SGR2017-1289). Z.L. is enrolled in the UAB
696 Ph.D. program and acknowledges the China Scholarship
697 Council (CSC) for his Ph.D. grant (201808310071).

698 ■ REFERENCES

- 699 (1) Long, J. R.; Yaghi, O. M. The Pervasive Chemistry of Metal-
700 Organic Frameworks. *Chem. Soc. Rev.* **2009**, *38*, 1213–1214.
- 701 (2) Kitagawa, S.; Kitaura, R.; Noro, S. Functional Porous
702 Coordination Polymers. *Angew. Chem., Int. Ed.* **2004**, *43*, 2334–2375.
- 703 (3) James, S. L. Metal–Organic Frameworks. *Chem. Soc. Rev.* **2003**,
704 *32*, 276–288.
- 705 (4) Li, H.; Eddaoudi, M.; O’Keeffe, M.; Yaghi, O. M. Design and
706 Synthesis of an Exceptionally Stable and Highly Porous Metal-
707 Organic Framework. *Nature* **1999**, *402*, 276–279.
- 708 (5) Dhaka, S.; Kumar, R.; Deep, A.; Kurade, M. B.; Ji, S.-W.; Jeon,
709 B.-H. Metal–Organic Frameworks (MOFs) for the Removal of
710 Emerging Contaminants from Aquatic Environments. *Coord. Chem.*
711 *Rev.* **2019**, *380*, 330–352.
- 712 (6) Du, M.; Li, Q.; Zhao, Y.; Liu, C.-S.; Pang, H. A Review of
713 Electrochemical Energy Storage Behaviors Based on Pristine Metal–
714 Organic Frameworks and Their Composites. *Coord. Chem. Rev.* **2020**,
715 *416*, No. 213341.
- 716 (7) Rojas, S.; Horcajada, P. Metal–Organic Frameworks for the
717 Removal of Emerging Organic Contaminants in Water. *Chem. Rev.*
718 **2020**, *120*, 8378–8415.
- 719 (8) Czaja, A. U.; Trukhan, N.; Müller, U. Industrial Applications of
720 Metal–Organic Frameworks. *Chem. Soc. Rev.* **2009**, *38*, 1284–1293.
- 721 (9) Cui, Y.; Yue, Y.; Qian, G.; Chen, B. Luminescent Functional
722 Metal–Organic Frameworks. *Chem. Rev.* **2012**, *112*, 1126–1162.
- 723 (10) Furukawa, H.; Cordova, K. E.; O’Keeffe, M.; Yaghi, O. M. The
724 Chemistry and Applications of Metal–Organic Frameworks. *Science*
725 **2013**, *341*, No. 1230444.
- 726 (11) Wang, H.; Zhu, Q.-L.; Zou, R.; Xu, Q. Metal–Organic
727 Frameworks for Energy Applications. *Chem* **2017**, *2*, 52–80.
- 728 (12) Lustig, W. P.; Mukherjee, S.; Rudd, N. D.; Desai, A. V.; Li, J.;
729 Ghosh, S. K. Metal–Organic Frameworks: Functional Luminescent
730 and Photonic Materials for Sensing Applications. *Chem. Soc. Rev.*
731 **2017**, *46*, 3242–3285.
- 732 (13) Espallargas, G. M.; Coronado, E. Magnetic Functionalities in
733 MOFs: From the Framework to the Pore. *Chem. Soc. Rev.* **2018**, *47*,
734 533–557.
- 735 (14) Armelao, L.; Quici, S.; Barigelli, F.; Accorsi, G.; Bottaro, G.;
736 Cavazzini, M.; Tondello, E. Design of Luminescent Lanthanide
737 Complexes: From Molecules to Highly Efficient Photo-Emitting
738 Materials. *Coord. Chem. Rev.* **2010**, *254*, 487–505.
- 739 (15) Xing, S.; Janiak, C. Design and Properties of Multiple-Emitter
740 Luminescent Metal–Organic Frameworks. *Chem. Commun.* **2020**, *56*,
741 12290–12306.
- 742 (16) Cui, Y.; Yue, Y.; Qian, G.; Chen, B. Luminescent Functional
743 Metal–Organic Frameworks. *Chem. Rev.* **2012**, *112*, 1126–1162.
- 744 (17) Eliseeva, S. V.; Bünzli, J.-C. G. Lanthanide Luminescence for
745 Functional Materials and Bio-Sciences. *Chem. Soc. Rev.* **2010**, *39*,
746 189–227.
- 747 (18) Rocha, J.; Carlos, L. D.; Paz, F. A. A.; Ananias, D. Luminescent
748 Multifunctional Lanthanides-Based Metal–Organic Frameworks.
749 *Chem. Soc. Rev.* **2011**, *40*, 926–940.
- 750 (19) Younis, S. A.; Bhardwaj, N.; Bhardwaj, S. K.; Kim, K.-H.; Deep,
751 A. R. Rare Earth Metal–Organic Frameworks (RE-MOFs): Synthesis,
752 Properties, and Biomedical Applications. *Coord. Chem. Rev.* **2021**,
753 *429*, No. 213620.
- 754 (20) Saraci, F.; Quezada-Novoa, V.; Donnarumma, P. R.; Howarth,
755 A. J. Rare-Earth Metal–Organic Frameworks: From Structure to
756 Applications. *Chem. Soc. Rev.* **2020**, *49*, 7949–7977.
- 757 (21) Gorai, T.; Schmitt, W.; Gunnlaugsson, T. Highlights of the
758 Development and Application of Luminescent Lanthanide Based
Coordination Polymers, MOFs and Functional Nanomaterials. *Dalton*
Trans. **2021**, *50*, 770–784.
- (22) Nguyen, T. N.; Eliseeva, S. V.; Gladysiak, A.; Petoud, S.;
Stylianou, K. C. Design of Lanthanide-Based Metal–Organic
Frameworks with Enhanced near-Infrared Emission. *J. Mater. Chem.*
A **2020**, *8*, 10188–10192.
- (23) Li, Z.; Liu, X.; Wang, G.; Li, B.; Chen, H.; Li, H.; Zhao, Y.
Photoresponsive Supramolecular Coordination Polyelectrolyte as
Smart Anticounterfeiting Inks. *Nat. Commun.* **2021**, *12*, No. 1363.
- (24) Abdollahi, A.; Roghani-Mamaqani, H.; Razavi, B.; Salami-
Kalajahi, M. Photoluminescent and Chromic Nanomaterials for
Anticounterfeiting Technologies: Recent Advances and Future
Challenges. *ACS Nano* **2020**, *14*, 14417–14492.
- (25) Gao, Z.; Yang, S.; Xu, B.; Zhang, T.; Chen, S.; Zhang, W.; Sun,
X.; Wang, Z.; Wang, X.; Meng, X.; Zhao, Y. S. Laterally Engineering
Lanthanide-MOFs Epitaxial Heterostructures for Spatially Resolved
Planar 2D Photonic Barcoding. *Angew. Chem.* **2021**, *133*, 24724–
24730.
- (26) Pei, K.; Wu, J.; Zhao, M.; Feng, X.; Li, Y.; Ma, Y.; Li, H.; Zhai,
T. Polarized Emission of Lanthanide Metal–Organic Framework (Ln-
MOF) Crystals for High-Capacity Photonic Barcodes. *Adv. Opt.*
Mater. **2022**, *10*, No. 2102143.
- (27) Zhou, H.; Han, J.; Cuan, J.; Zhou, Y. Responsive Luminescent
MOF Materials for Advanced Anticounterfeiting. *Chem. Eng. J.* **2022**,
431, No. 134170.
- (28) Burtch, N. C.; Jasuja, H.; Walton, K. S. Water Stability and
Adsorption in Metal–Organic Frameworks. *Chem. Rev.* **2014**, *114*,
10575–10612.
- (29) Rieth, A. J.; Hunter, K. M.; Dincă, M.; Paesani, F. Hydrogen
Bonding Structure of Confined Water Templated by a Metal–Organic
Framework with Open Metal Sites. *Nat. Commun.* **2019**, *10*,
No. 4771.
- (30) Ding, M.; Cai, X.; Jiang, H.-L. Improving MOF Stability:
Approaches and Applications. *Chem. Sci.* **2019**, *10*, 10209–10230.
- (31) Yuan, S.; Feng, L.; Wang, K.; Pang, J.; Bosch, M.; Lollar, C.;
Sun, Y.; Qin, J.; Yang, X.; Zhang, P.; Wang, Q. Stable Metal–Organic
Frameworks: Design, Synthesis, and Applications. *Adv. Mater.* **2018**,
30, No. 1704303.
- (32) Zhang, X.; Wang, B.; Alsalmeh, A.; Xiang, S.; Zhang, Z.; Chen, B.
Design and Applications of Water-Stable Metal–Organic Frameworks:
Status and Challenges. *Coord. Chem. Rev.* **2020**, *423*, No. 213507.
- (33) Liu, X.; Wang, X.; Kapteijn, F. Water and Metal–Organic
Frameworks: From Interaction toward Utilization. *Chem. Rev.* **2020**,
120, 8303–8377.
- (34) Duan, J.; Jin, W.; Kitagawa, S. Water-Resistant Porous
Coordination Polymers for Gas Separation. *Coord. Chem. Rev.* **2017**,
332, 48–74.
- (35) Gelfand, B. S.; Shimizu, G. K. H. Parameterizing and Grading
Hydrolytic Stability in Metal–Organic Frameworks. *Dalton Trans.*
2016, *45*, 3668–3678.
- (36) Yu, H.; Liu, Q.; Li, J.; Su, Z.-M.; Li, X.; Wang, X.; Sun, J.; Zhou,
C.; Hu, X. A Dual-Emitting Mixed-Lanthanide MOF with High
Water-Stability for Ratiometric Fluorescence Sensing of Fe³⁺ and
Ascorbic Acid. *J. Mater. Chem. C* **2021**, *9*, 562–568.
- (37) Plešek, J. Potential Applications of the Boron Cluster
Compounds. *Chem. Rev.* **1992**, *92*, 269–278.
- (38) Scholz, M.; Hey-Hawkins, E. Carboranes as Pharmaco-
phores: Properties, Synthesis, and Application Strategies. *Chem. Rev.*
2011, *111*, 7035–7062.
- (39) Grimes, R. N. *Carboranes*; Grimes, R. N., Ed.; Academic Press,
2016.
- (40) Teixidor, F.; Kaufmann, D. E. *Science of Synthesis: Houben-Weyl*
Methods of Molecular Transformations, 5th ed.; Mulzer, Ed.; Georg
Thieme Verlag: Stuttgart, 2015; Vol. 6.
- (41) Fujii, S. Expanding the Chemical Space of Hydrophobic
Pharmacophores: The Role of Hydrophobic Substructures in the
Development of Novel Transcription Modulators. *MedChemComm*
2016, *7*, 1082–1092.

- 827 (42) Issa, F.; Kassiou, M.; Rendina, L. M. Boron in Drug Discovery: 828 Carboranes as Unique Pharmacophores in Biologically Active 829 Compounds. *Chem. Rev.* **2011**, *111*, 5701–5722.
- 830 (43) Valliant, J. F.; Guenther, K. J.; King, A. S.; Morel, P.; Schaffer, 831 P.; Sogbein, O. O.; Stephenson, K. A. The Medicinal Chemistry of 832 Carboranes. *Coord. Chem. Rev.* **2002**, *232*, 173–230.
- 833 (44) Farha, O. K.; Spokoyny, A. M.; Mulfort, K. L.; Hawthorne, M. 834 F.; Mirkin, C. A.; Hupp, J. T. Synthesis and Hydrogen Sorption 835 Properties of Carborane Based Metal–Organic Framework Materials. 836 *J. Am. Chem. Soc.* **2007**, *129*, 12680–12681.
- 837 (45) Bae, Y.-S.; Farha, O. K.; Spokoyny, A. M.; Mirkin, C. A.; Hupp, 838 J. T.; Snurr, R. Q. Carborane-Based Metal–Organic Frameworks as 839 Highly Selective Sorbents for CO₂ over Methane. *Chem. Commun.* 840 **2008**, No 35, 4135.
- 841 (46) Farha, O. K.; Spokoyny, A. M.; Mulfort, K. L.; Galli, S.; Hupp, 842 J. T.; Mirkin, C. A. Gas-Sorption Properties of Cobalt(II)– 843 Carborane-Based Coordination Polymers as a Function of Morphol- 844 ogy. *Small* **2009**, *5*, 1727–1731.
- 845 (47) Bae, Y.-S.; Spokoyny, A. M.; Farha, O. K.; Snurr, R. Q.; Hupp, 846 J. T.; Mirkin, C. A. Separation of Gas Mixtures Using Co(II) 847 Carborane-Based Porous Coordination Polymers. *Chem. Commun.* 848 **2010**, *46*, 3478–3480.
- 849 (48) Spokoyny, A. M.; Farha, O. K.; Mulfort, K. L.; Hupp, J. T.; 850 Mirkin, C. A. Porosity Tuning of Carborane-Based Metal–Organic 851 Frameworks (MOFs) via Coordination Chemistry and Ligand 852 Design. *Inorg. Chim. Acta* **2010**, *364*, 266–271.
- 853 (49) Huang, S.-L.; Lin, Y.-J.; Yu, W.-B.; Jin, G.-X. Porous 854 Frameworks Based on Carborane-Ln₂(CO₂)₆: Architecture Influ- 855 enced by Lanthanide Contraction and Selective CO₂ Capture. 856 *ChemPlusChem* **2012**, *77*, 141–147.
- 857 (50) Kennedy, R. D.; Krungleviciute, V.; Clingerman, D. J.; 858 Mondloch, J. E.; Peng, Y.; Wilmer, C. E.; Sarjeant, A. A.; Snurr, R. 859 Q.; Hupp, J. T.; Yildirim, T.; Farha, O. K.; Mirkin, C. A. Carborane- 860 Based Metal–Organic Framework with High Methane and Hydrogen 861 Storage Capacities. *Chem. Mater.* **2013**, *25*, 3539–3543.
- 862 (51) Clingerman, D. J.; Morris, W.; Mondloch, J. E.; Kennedy, R. D.; 863 Sarjeant, A. A.; Stern, C.; Hupp, J. T.; Farha, O. K.; Mirkin, C. A. 864 Stabilization of a Highly Porous Metal–Organic Framework Utilizing 865 a Carborane-Based Linker. *Chem. Commun.* **2015**, *51*, 6521–6523.
- 866 (52) Planas, J.; Teixidor, F.; Viñas, C. N,O-Type Carborane-Based 867 Materials. *Crystals* **2016**, *6*, 50.
- 868 (53) Di Salvo, F.; Paterakis, C.; Tsang, M. Y.; Garcia, Y.; Viñas, C.; 869 Teixidor, F.; Giner Planas, J.; Light, M. E.; Hursthouse, M. B.; 870 Choquesillo-Lazarte, D. Synthesis and Crystallographic Studies of 871 Disubstituted Carboranyl Alcohol Derivatives: Prevailing Chiral 872 Recognition? *Cryst. Growth Des.* **2013**, *13*, 1473–1484.
- 873 (54) Di Salvo, F.; Tsang, M. Y.; Teixidor, F.; Viñas, C.; Planas, J. G.; 874 Crassous, J.; Vanthuyne, N.; Aliaga-Alcalde, N.; Ruiz, E.; Coquerel, 875 G.; Clevers, S.; Dupray, V.; Choquesillo-Lazarte, D.; Light, M. E.; 876 Hursthouse, M. B. A Racemic and Enantiopure Unsymmetric 877 Diiron(III) Complex with a Chiral o-Carborane-Based Pyridylalcohol 878 Ligand: Combined Chiroptical, Magnetic, and Nonlinear Optical 879 Properties. *Chem. - Eur. J.* **2014**, *20*, 1081–1090.
- 880 (55) Tsang, M. Y.; Viñas, C.; Teixidor, F.; Planas, J. G.; Conde, N.; 881 SanMartin, R.; Herrero, M. T.; Dominguez, E.; Lledos, A.; Vidossich, 882 P.; Choquesillo-Lazarte, D. Synthesis, Structure, and Catalytic 883 Applications for Ortho- and Meta-Carboranyl Based NBN Pincer- 884 Pd Complexes. *Inorg. Chem.* **2014**, *53*, 9284–9295.
- 885 (56) Tsang, M. Y.; Teixidor, F.; Viñas, C.; Choquesillo-Lazarte, D.; 886 Aliaga-Alcalde, N.; Planas, J. G. Synthesis, Structures and Properties 887 of Iron(III) Complexes with (o-Carboranyl)Bis-(2-Hydroxymethyl)- 888 Pyridine: Racemic versus Meso. *Inorg. Chim. Acta* **2016**, *448*, 97–103.
- 889 (57) Soldevila-Sanmartín, J.; Ruiz, E.; Choquesillo-Lazarte, D.; 890 Light, M. E.; Viñas, C.; Teixidor, F.; Núñez, R.; Pons, J.; Planas, J. G. 891 Tuning the Architectures and Luminescence Properties of Cu- 892 (<sc>i>/sc>) Compounds of Phenyl and Carboranyl Pyrazoles: 893 The Impact of 2D versus 3D Aromatic Moieties in the Ligand 894 Backbone. *J. Mater. Chem. C* **2021**, *9*, 7643–7657.
- (58) Rodríguez-Hermida, S.; Tsang, M. Y.; Vignatti, C.; Stylianou, 895 K. C.; Guillerm, V.; Pérez-Carvajal, J.; Teixidor, F.; Viñas, C.; 896 Choquesillo-Lazarte, D.; Verdugo-Escamilla, C.; Peral, I.; Juanhuix, J.; 897 Verdaguier, A.; Imaz, I.; Maspocho, D.; Giner Planas, J. Switchable 898 Surface Hydrophobicity-Hydrophilicity of a Metal–Organic Frame- 899 work. *Angew. Chem., Int. Ed.* **2016**, *55*, 16049–16053. 900
- (59) Tsang, M. Y.; Rodríguez-Hermida, S.; Stylianou, K. C.; Tan, F.; 901 Negi, D.; Teixidor, F.; Viñas, C.; Choquesillo-Lazarte, D.; Verdugo- 902 Escamilla, C.; Guerrero, M.; Sort, J.; Juanhuix, J.; Maspocho, D.; Giner 903 Planas, J. Carborane Bis-Pyridylalcohols as Linkers for Coordination 904 Polymers: Synthesis, Crystal Structures, and Guest-Framework 905 Dependent Mechanical Properties. *Cryst. Growth Des.* **2017**, *17*, 906 846–857. 907
- (60) Tan, F.; López-Periago, A.; Light, M. E.; Cirera, J.; Ruiz, E.; 908 Borrás, A.; Teixidor, F.; Viñas, C.; Domingo, C.; Planas, J. G. An 909 Unprecedented Stimuli-Controlled Single-Crystal Reversible Phase 910 Transition of a Metal–Organic Framework and Its Application to a 911 Novel Method of Guest Encapsulation. *Adv. Mater.* **2018**, *30*, 912 No. 1800726. 913
- (61) Gan, L.; Chidambaram, A.; Fonquernie, P. G.; Light, M. E.; 914 Choquesillo-Lazarte, D.; Huang, H.; Solano, E.; Fraile, J.; Viñas, C.; 915 Teixidor, F.; Navarro, J. A. R.; Stylianou, K. C.; Planas, J. G. A Highly 916 Water-Stable Meta-Carborane-Based Copper Metal–Organic Frame- 917 work for Efficient High-Temperature Butanol Separation. *J. Am.* 918 *Chem. Soc.* **2020**, *142*, 8299–8311. 919
- (62) Li, Z.; Fraile, J.; Viñas, C.; Teixidor, F.; Planas, J. G. Post- 920 Synthetic Modification of a Highly Flexible 3D Soft Porous Metal– 921 Organic Framework by Incorporating Conducting Polypyrrole: 922 Enhanced MOF Stability and Capacitance as an Electrode Material. 923 *Chem. Commun.* **2021**, *57*, 2523–2526. 924
- (63) Li, Z.; Choquesillo-Lazarte, D.; Fraile, J.; Viñas, C.; Teixidor, 925 F.; Planas, J. G. Rational Design of Carborane-Based Cu₂-Paddle 926 Wheel Coordination Polymers for Increased Hydrolytic Stability. 927 *Dalton Trans.* **2022**, *51*, 1137–1143. 928
- (64) Teixidor, F.; Barberà, G.; Vaca, A.; Kivekäs, R.; Sillanpää, R.; 929 Oliva, J.; Viñas, C. Are Methyl Groups Electron-Donating or 930 Electron-Withdrawing in Boron Clusters? Permethylation of o- 931 Carborane. *J. Am. Chem. Soc.* **2005**, *127*, 10158–10159. 932
- (65) Poater, J.; Viñas, C.; Bennour, I.; Escayola, S.; Solà, M.; 933 Teixidor, F. Too Persistent to Give Up: Aromaticity in Boron Clusters 934 Survives Radical Structural Changes. *J. Am. Chem. Soc.* **2020**, *142*, 935 9396–9407. 936
- (66) Bellomo, C.; Zanetti, D.; Cardano, F.; Sinha, S.; Chaari, M.; 937 Fin, A.; Maranzana, A.; Núñez, R.; Blangetti, M.; Prandi, C. Red 938 Light-Emitting Carborane-BODIPY Dyes: Synthesis and Properties of 939 Visible-Light Tuned Fluorophores with Enhanced Boron Content. 940 *Dyes Pigm.* **2021**, *194*, No. 109644. 941
- (67) Ferrer-Ugalde, A.; González-Campo, A.; Planas, J. G.; Viñas, C.; 942 Teixidor, F.; Sáez, I. M.; Núñez, R. Tuning the Liquid Crystallinity of 943 Cholesteryl-o-Carborane Dyads: Synthesis, Structure, Photolumines- 944 cence, and Mesomorphic Properties. *Crystals* **2021**, *11*, 133. 945
- (68) Chaari, M.; Kelemen, Z.; Choquesillo-Lazarte, D.; 946 Gaztelumendi, N.; Teixidor, F.; Viñas, C.; Nogués, C.; Núñez, R. 947 Efficient Blue Light Emitting Materials Based on M-Carborane– 948 Anthracene Dyads. Structure, Photophysics and Bioimaging Studies. 949 *Biomater. Sci.* **2019**, *7*, 5324–5337. 950
- (69) Bellomo, C.; Chaari, M.; Cabrera-González, J.; Blangetti, M.; 951 Lombardi, C.; Deagostino, A.; Viñas, C.; Gaztelumendi, N.; Nogués, 952 C.; Núñez, R.; Prandi, C. Carborane-BODIPY Dyads: New 953 Photoluminescent Materials through an Efficient Heck Coupling. 954 *Chem. - Eur. J.* **2018**, *24*, 15622–15630. 955
- (70) Chaari, M.; Kelemen, Z.; Planas, J. G.; Teixidor, F.; 956 Choquesillo-Lazarte, D.; Ben Salah, A.; Viñas, C.; Núñez, R. 957 Photoluminescence in M-Carborane–Anthracene Triads: A Com- 958 bined Experimental and Computational Study. *J. Mater. Chem. C* 959 **2018**, *6*, 11336–11347. 960
- (71) Ferrer-Ugalde, A.; Cabrera-González, J.; Juárez-Pérez, E. J.; 961 Teixidor, F.; Pérez-Inestrosa, E.; Montenegro, J. M.; Sillanpää, R.; 962 Haukka, M.; Núñez, R. Carborane–Stilbene Dyads: The Influence of 963

- 964 Substituents and Cluster Isomers on Photoluminescence Properties. *Dalton Trans.* **2017**, 46, 2091–2104.
- 966 (72) Cabrera-González, J.; Viñas, C.; Haukka, M.; Bhattacharyya, S.; Gierschner, J.; Núñez, R. Photoluminescence in Carborane–Stilbene Triads: A Structural, Spectroscopic, and Computational Study. *Chem. Eur. J.* **2016**, 22, 13588–13598.
- 970 (73) Ferrer-Ugalde, A.; González-Campo, A.; Viñas, C.; Rodríguez-Romero, J.; Santillan, R.; Farfán, N.; Sillanpää, R.; Sousa-Pedraes, A.; Núñez, R.; Teixidor, F. Fluorescence of New O-Carborane Compounds with Different Fluorophores: Can It Be Tuned? *Chem. Eur. J.* **2014**, 20, 9940–9951.
- 975 (74) Ferrer-Ugalde, A.; Juárez-Pérez, E. J.; Teixidor, F.; Viñas, C.; Sillanpää, R.; Pérez-Inestrosa, E.; Núñez, R. Synthesis and Characterization of New Fluorescent Styrene-Containing Carborane Derivatives: The Singular Quenching Role of a Phenyl Substituent. *Chem. Eur. J.* **2012**, 18, 544–553.
- 980 (75) Lerouge, F.; Viñas, C.; Teixidor, F.; Núñez, R.; Abreu, A.; Xochitiotzi, E.; Santillan, R.; Farfán, N. High Boron Content Carboranyl-Functionalized Aryl Ether Derivatives Displaying Photoluminescent Properties. *Dalton Trans.* **2007**, 19, 1898–1903.
- 984 (76) Núñez, R.; Romero, L.; Teixidor, F.; Viñas, C. Icosahedral Boron Clusters: A Perfect Tool for the Enhancement of Polymer Features. *Chem. Soc. Rev.* **2016**, 45, 5147–5173.
- 987 (77) Hosmane, N. S. *Boron Science: New Technologies and Applications*; CRC Press, 2016.
- 989 (78) Dash, B. P.; Satapathy, R.; Maguire, J. A.; Hosmane, N. S. Polyhedral Boron Clusters in Materials Science. *New J. Chem.* **2011**, 35, 1955–1972.
- 992 (79) Mukherjee, S.; Thilagar, P. Boron Clusters in Luminescent Materials. *Chem. Commun.* **2016**, 52, 1070–1093.
- 994 (80) Zhang, H.; Li, W.; Yan, X.; Cai, W.; Li, M.; He, R.; Shen, W. Electronic Structure and Luminescence Properties of Unique Complexes: Cyclometalated Iridium(III) Chelated by: O-Carboranyl-Pyridine Ligands. *New J. Chem.* **2018**, 42, 5955–5966.
- 998 (81) Xu, W.-J.; Qin, Y.-Y.; Wei, L.-W.; Zhang, K. Y.; Liu, S.-J.; Zhao, Q. Boron-Functionalized Phosphorescent Iridium(III) Complexes. *Eur. J. Inorg. Chem.* **2017**, 2017, 4393–4405.
- 1001 (82) Xia, Q.; Zhang, J.; Chen, X.; Cheng, C.; Chu, D.; Tang, X.; Li, M. H.; Cui, Y. Synthesis, Structure and Property of Boron-Based Metal–Organic Materials. *Coord. Chem. Rev.* **2021**, 435, No. 213783.
- 1004 (83) Wang, J.-J.; Si, P.-P.; Liu, M.-J.; Chen, Y.; Yu, S.-X.; Lu, M.; Wang, S.-Y.; Li, B.; Li, P.-P.; Zhang, R.-C. Selective Fluorescent Sensing and Photodegradation Properties of Tb(III)-Based MOFs with Different Bulky Backbone Ligands. *Polyhedron* **2019**, 157, 63–108.
- 1009 (84) Sun, M.-L.; Zhang, J.; Lin, Q.-P.; Yin, P.-X.; Yao, Y.-G. Multifunctional Homochiral Lanthanide Camphorates with Mixed Achiral Terephthalate Ligands. *Inorg. Chem.* **2010**, 49, 9257–9264.
- 1012 (85) Zhao, Z.-P.; Zheng, K.; Li, H.-R.; Zeng, C.-H.; Zhong, S.; Ng, S. W.; Zheng, Y.; Chen, Y. Structure Variation and Luminescence of 3D, 2D and 1D Lanthanide Coordination Polymers with 1,3-Adamantanediacyetic Acid. *Inorg. Chim. Acta* **2018**, 482, 340–346.
- 1016 (86) Li, Y.; Wang, N.; Xiong, Y.-J.; Cheng, Q.; Fang, J.-F.; Zhu, F.-F.; Long, Y.; Yue, S.-T. Lanthanide Metal–Organic Frameworks Based on the 4,4'-Oxybisbenzoic Acid Ligand: Synthesis, Structures and Physical Properties. *New J. Chem.* **2015**, 39, 9872–9878.
- 1020 (87) Cui, Y.; Zhang, J.; Chen, B.; Qian, G. Chapter 290 - Lanthanide Metal–Organic Frameworks for Luminescent Applications. In *Including Actinides*, Bünzli, J.-C. G.; Pecharsky, V. K., Eds.; Handbook on the Physics and Chemistry of Rare Earths; 2016; Vol. 50, pp 243–268.
- 1025 (88) de Lill, D. T.; de Bettencourt-Dias, A.; Cahill, C. L. Exploring Lanthanide Luminescence in Metal–Organic Frameworks: Synthesis, Structure, and Guest-Sensitized Luminescence of a Mixed Europium/Terbium-Adipate Framework and a Terbium-Adipate Framework. *Inorg. Chem.* **2007**, 46, 3960–3965.
- 1030 (89) Ma, L.-L.; Yang, G.-P.; Li, G.-P.; Zhang, P.-F.; Jin, J.; Wang, Y.; Wang, J.-M.; Wang, Y.-Y. Luminescence Modulation, near White Light Emission, Selective Luminescence Sensing, and Anticounterfeiting via a Series of Ln-MOFs with a π -Conjugated and Uncoordinated Lewis Basic Triazolyl Ligand. *Inorg. Chem. Front.* **2021**, 8, 329–338.
- 1034 (90) Lustig, W. P.; Li, J. Luminescent Metal–Organic Frameworks and Coordination Polymers as Alternative Phosphors for Energy Efficient Lighting Devices. *Coord. Chem. Rev.* **2018**, 373, 116–147.
- 1037 (91) Mohapatra, S.; Adhikari, S.; Rijju, H.; Maji, T. K. Terbium(III), Europium(III), and Mixed Terbium(III)–Europium(III) Muciccate Frameworks: Hydrophilicity and Stoichiometry-Dependent Color Tunability. *Inorg. Chem.* **2012**, 51, 4891–4893.
- 1042 (92) Chen, D.-H.; Haldar, R.; Neumeier, B. L.; Fu, Z.-H.; Feldmann, C.; Wöll, C.; Redel, E. Tunable Emission in Heteroepitaxial Ln-SURMOFs. *Adv. Funct. Mater.* **2019**, 29, No. 1903086.
- 1044 (93) Zhang, J.-C.; Pan, C.; Zhu, Y.-F.; Zhao, L.-Z.; He, H.-W.; Liu, X.; Qiu, J. Achieving Thermo-Mechano-Opto-Responsive Bitemporal Colorful Luminescence via Multiplexing of Dual Lanthanides in Piezoelectric Particles and Its Multidimensional Anticounterfeiting. *Adv. Mater.* **2018**, 30, No. 1804644.
- 1049 (94) Pan, M.; Zhu, Y.-X.; Wu, K.; Chen, L.; Hou, Y.-J.; Yin, S.-Y.; Wang, H.-P.; Fan, Y.-N.; Su, C.-Y. Epitaxial Growth of Hetero-Ln-MOF Hierarchical Single Crystals for Domain- and Orientation-Controlled Multicolor Luminescence 3D Coding Capability. *Angew. Chem., Int. Ed.* **2017**, 56, 14582–14586.
- 1054 (95) Zhao, Y.-W.; Zhang, F.-Q.; Zhang, X.-M. Single Component Lanthanide Hybrids Based on Metal–Organic Framework for Near-Ultraviolet White Light LED. *ACS Appl. Mater. Interfaces* **2016**, 8, 24123–24130.
- 1058 (96) Ramya, A. R.; Sharma, D.; Natarajan, S.; Reddy, M. L. P. Highly Luminescent and Thermally Stable Lanthanide Coordination Polymers Designed from 4-(Dipyridin-2-Yl)Aminobenzoate: Efficient Energy Transfer from Tb³⁺ to Eu³⁺ in a Mixed Lanthanide Coordination Compound. *Inorg. Chem.* **2012**, 51, 8818–8826.
- 1063 (97) Im, W. B.; Brinkley, S.; Hu, J.; Mikhailovsky, A.; DenBaars, S. P.; Seshadri, R. Sr₂975-xBaxCe_{0.025}AlO₄F: A Highly Efficient Green-Emitting Oxyfluoride Phosphor for Solid State White Lighting. *Chem. Mater.* **2010**, 22, 2842–2849.
- 1067 (98) Ou, Y.; Zhou, W.; Zhu, Z.; Ma, F.; Zhou, R.; Su, F.; Zheng, L.; Ma, L.; Liang, H. Host Differential Sensitization toward Color/Lifetime-Tuned Lanthanide Coordination Polymers for Optical Multiplexing. *Angew. Chem., Int. Ed.* **2020**, 59, 23810–23816.
- 1071 (99) Xie, Y.; Arno, M. C.; Husband, J. T.; Torrent-Sucarrat, M.; O'Reilly, R. K. Manipulating the Fluorescence Lifetime at the Sub-Cellular Scale via Photo-Switchable Barcoding. *Nat. Commun.* **2020**, 11, No. 2460.
- 1075 (100) Deneff, J. I.; Butler, K. S.; Rohwer, L. E. S.; Pearce, C. J.; Valdez, N. R.; Rodriguez, M. A.; Luk, T. S.; Sava Gallis, D. F. Encoding Multilayer Complexity in Anti-Counterfeiting Heterometallic MOF-Based Optical Tags. *Angew. Chem., Int. Ed.* **2021**, 60, 1203–1211.
- 1080 (101) Fox, M. A. Icosahedral Carborane Derivatives. Ph.D. Thesis, Durham University, 1991.
- 1082 (102) Sheldrick, G. M. SHELXT-Integrated Space-Group and Crystal-Structure Determination. *Acta Crystallogr., Sect. A: Found. Adv.* **2015**, 71, 3–8.
- 1085 (103) Dolomanov, O. V.; Bourhis, L. J.; Gildea, R. J.; Howard, J. A. K.; Puschmann, H. OLEX2: A Complete Structure Solution, Refinement and Analysis Program. *J. Appl. Crystallogr.* **2009**, 42, 339–341.
- 1089 (104) Sheldrick, G. M. Crystal Structure Refinement with SHELXL. *Acta Crystallogr., Sect. C: Struct. Chem.* **2015**, 71, 3–8.
- 1091